

AN ANALYTICAL AND EXPERIMENTAL
STUDY OF HEAT AND MOMENTUM
TRANSFER IN TURBULENT SEPARATED
FLOW PAST A RECTANGULAR CAVITY

Thesis for the Degree of Ph. D.
MICHIGAN STATE UNIVERSITY

Ronald L. Haugen

1966

THESIS

e, 2



3 1293 20097 7761

LIBRARY
Michigan State
University

ABSTRACT

AN ANALYTICAL AND EXPERIMENTAL STUDY OF HEAT AND MOMENTUM TRANSFER IN TURBULENT SEPARATED FLOW PAST A RECTANGULAR CAVITY

by Ronald L. Haugen

The study given here presents results of an analytical and experimental investigation aimed at describing the turbulent heat and momentum transfer mechanism in the separated flow region of a transverse rectangular cavity facing an oncoming boundary layer.

A flow model of the mixing region in the slot postulated on the basis of eddy diffusion gives values of velocity, temperature, drag, and heat transfer in good agreement with experimental measurements. In each case, experiments were conducted with air at Reynolds numbers up to 1.3×10^6 , cavity height to width ratios from 0.2 to 4.5, and with aspect ratios exceeding 10. The results further point to the significant effects exerted by the oncoming boundary layer on transfer rates from the slot.

It was found that the average Stanton number is represented by the semi-theoretical correlation equation

$$\bar{St} = 0.0365 (\delta/b)^{-0.1367} \pm 15\% \quad \text{for } \delta/b \text{ (ratio of boundary}$$

layer thickness to slot width) ranging from 0.1 to 0.8.

AN ANALYTICAL AND EXPERIMENTAL STUDY OF
HEAT AND MOMENTUM TRANSFER IN TURBULENT
SEPARATED FLOW PAST A RECTANGULAR CAVITY

By

Ronald L.^c Haugen

A THESIS

Submitted to
Michigan State University
in partial fulfillment of the requirements
for the degree of

DOCTOR OF PHILOSOPHY

Department of Mechanical Engineering

1966

ACKNOWLEDGMENTS

The author wishes to express his sincere appreciation and thanks to his major professor, Dr. Amritlal M. Dhanak, for his generous help and encouragement which made this thesis possible.

Special thanks are also extended to Dr. Joachim E. Lay (Mechanical Engineering), Dr. Edward A. Nordhaus (Mathematics), and Dr. Terry Triffet (Metalurgy, Mechanics, and Material Science) for serving on the guidance committee.

Finally, the author acknowledges that this thesis, indeed his entire graduate program, would not have been possible without the patience, understanding, and consistent encouragement of his wife, Mary.

R. J.

TABLE OF CONTENTS

	Page
ACKNOWLEDGMENTS	ii
LIST OF FIGURES	iv
NOMENCLATURE	vii
1. INTRODUCTION	1
2. EXPERIMENTAL STUDIES	6
2.1 Description of Test Equipment	6
2.2 Instrumentation and Measurements	11
3. ANALYTICAL STUDIES	19
3.1 Analytical Flow Model	19
3.2 Basic Equations	20
3.3 Solution of Momentum Equation	21
3.4 Solution of Energy Equation	33
4. ANALYTICAL AND EXPERIMENTAL RESULTS	41
4.1 Flow Patterns	41
4.2 Pressure	41
4.3 Velocity	48
4.4 Turbulence	52
4.5 Temperature	55
4.6 Heat Transfer	62
5. CONCLUSIONS	72
REFERENCES	74
APPENDIX	76

LIST OF FIGURES

Figure		Page
1.	Physical Flow Model	7
2.	Test Equipment	8
3.	Flow Channel and Traversing Mechanism	9
4.	Schematic Diagram of Test Rig Used for Measuring Heat Transfer Rates	12
5.	Test Equipment	13
6.	Typical Calibration Curve for the Hot-wire Anemometer	16
7.	Water Flow Model	18
8.	A Typical Distribution of the Quantities $\sqrt{u'^2}/\bar{u}$ and $\overline{u'v'}/\bar{u}^2$ ($h/b = 1.0$)	24
9.	Constants k_1 , k_2 , and k_3 of Equation (3.22)	27
10.	Constants C_1 and C_2 of Equation (3.29)	29
11.	Velocity Distribution for $x/b = .15$	30
12.	Velocity Distribution for $x/b = .50$	31
13.	Velocity Distribution for $x/b = .85$	32
14.	Typical Distribution of ϵ_m for $x/b = 0.50$	38
15.	Factor K of Equation (3.38)	39

Figure		Page
16.	Pictures of Flow Patterns in Cavity with (a) $h/b = 1.0$ (b) $h/b = 1.5$ (c) $h/b = 1.75$	42
17.	Pictures of Flow Patterns in Cavity with (a) $h/b = 2.0$ (b) $h/b = 2.5$ (c) $h/b = 3.0$	43
18.	Measured Pressure Distributions Along Cavity Wall Showing Influences of Height to Width Ratio	45
19.	Typical Longitudinal Pressure Distribution in the Shear Layer (at $y = 0$)	46
20.	Predicted Effect of the Oncoming Boundary Layer Thickness of the Turbulent Shear Stress and Com- parison with Experiment	47
21.	Comparison of Experimental and Analytical Velocity Profiles ($x/b = 0.15$)	49
22.	Comparison of Experimental and Analytical Velocity Profiles ($s/b = 0.50$)	50
23.	Comparison of Experimental and Analytical Velocity Profiles ($s/b = 0.85$)	51
24.	Plot of Cavity Streamlines Calculated from the Analysis ($h/b = 1/0, \delta/b = 0.1$)	53
25.	Turbulence Intensity and Shear Distributions ($h/b = 1.0$)	54
26.	Temperature Profiles for $h/b = 1.0$ and $\delta/b = .28$	56
27.	Temperature Profiles for $h/b = 1.0$ and $\delta/b = .58$	57
28.	Temperature Profiles for $h/b = 1.5$ and $\delta/b = .56$	58
29.	Temperature Profiles for $h/b = 1.5$ and $\delta/b = .79$	59

Figure		Page
30.	Temperature Profiles for $h/b = 2.0$ and $\delta/b = .38$	60
31.	Temperature Profiles for $h/b = 2.0$ and $\delta/b = .76$	61
32.	Predicted Cavity Bulk Temperature and Comparison with Experimental Data	63
33.	Predicted and Measured Temperature Profiles ($h/b = 0.5$, $\delta/b = 0.21$)	64
34.	Predicted and Measured Temperature Profiles ($h/b = 1.0$, $\delta/b = 0.28$)	65
35.	Predicted and Measured Temperature Profiles ($h/b = 1.0$, $\delta/b = 0.58$)	66
36.	Predicted and Measured Temperature Profiles ($h/b = 1.0$, $\delta/b = 0.76$)	67
37.	Local Cavity Heat Transfer Rates ($h/b = 1.0$) .	69
38.	Average Heat Transfer from a Heated Cavity (Data Based on Average Heat Transfer Rates) .	70
39.	Average Heat Transfer from a Heated Cavity (Data Based on Local Heat Transfer Rates). .	71

NOMENCLATURE

A	constant defined in equation (3.33)
b	cavity width, ft.
c_p	specific heat, BTU/lb _f . °F
C_p	pressure coefficient
h	cavity depth, ft.
\bar{h}	average film coefficient, BTU/hr. ft. ² °F
k	thermal conductivity, BTU/hr. ft. °F
P	static pressure, lb _f ./ft. ²
\bar{q}	average heat transfer, BTU/ft. ² hr.
St	Stanton number
T'	fluctuating component of temperature, °F
\bar{T}	time-mean temperature, °F
\bar{u}	x-component of time mean velocity, ft./sec.
u'	fluctuating x-component of velocity, ft./sec.
\bar{v}	y-component of time mean velocity, ft./sec.
v'	fluctuating y-component of velocity, ft./sec.

x	coordinate along dividing streamline, ft.
y	coordinate normal to dividing streamline, ft.
δ	thickness of boundary layer at the leading edge, ft.
ϵ_h	eddy diffusivity of heat, ft^2/hr .
ϵ_m	eddy diffusivity of momentum, ft^2/hr .
η	transformed coordinate
ϕ	transformed coordinate
ψ	stream function
ρ	fluid density, lb_m/ft^3 .
τ	shear stress, lb_f/ft^2 .

SUBSCRIPTS

w	wall conditions
o	average inviscid core conditions
∞	free stream condition

1. INTRODUCTION

Separated flows occur, for example, where indentations or proturbances are present on flow surfaces. In view of the importance of such related flows to the design of aerodynamic surfaces, considerable attention has been drawn to the mechanism of flow separation. The boundary layer separation is characterized by the formation of reverse flows and vortices. Fox (1) showed that a shear layer like that of a free jet boundary forms over the cavity and borders the external flow. It widens from the front to the back of the cavity and part of this free shear layer is deflected into the notch at the back edge, giving rise to the flow within the cavity. In particular, the boundary layer (laminar or turbulent) separating at the leading edge of a cavity subsequently reattaches itself either at the recompression corner or at the base. This, as discovered by Charwat (2), depends largely upon the depth to width ratio, the oncoming boundary layer thickness, and the relative heights of the forward and rear steps. In the case of a fairly narrow slot, evidence suggests that the boundary layer "bridges" the notch. Charwat's data reveal that the oncoming boundary layer thickness and the free stream Mach number are important parameters, primarily in the case of the cavity closure. The pressure and thermal measurements presented by Charwat were for

the bottom of rectangular cavities with height to length ratios (h/b) smaller than four. Pressures in the turbulent subsonic flow were shown to rise above the free stream pressure in the downstream end of the cavity and to be little affected in the upstream end.

Larson (4) measured the average heat transfer coefficients for both laminar and turbulent flow in cavities substantially rectangular in shape and having height to length ratios of 0.208 and less. For laminar flow, the average heat transfer coefficient was found to be about 56% of the average coefficient that was measured on equivalent models with a straight heated portion replacing the cavity. For turbulent flow, the average coefficient was proportional to $(\rho_{\infty} u_{\infty})^{0.6}$. However, no simple ratio (as the 56% for laminar flows) exists between this flow and that of the straight heated portion.

Some additional quantitative results are reported in papers by Wieghardt (5) and by Tillman (6). Their studies of flow past cavities consisted of measuring the overall drag coefficients, these being obtained by subtracting the drag values with and without a surface cutout.

Flow measurements in a rectangular cutout were also made by Roshko (7). His results consist of pressure, velocity, and skin friction measurements on the cavity walls with emphasis on the effects of varying the cavity depth-breadth ratio. Roshko's work,

completely experimental in nature, gives rise to a number of tentative conclusions regarding the prominent aspects of the flow in slots.

Most importantly:

1. The pressures and forces due to the flow may be expected to depend on the state of the boundary layer ahead of the cavity.

2. The drag increment due to a cavity is almost entirely accounted for by the pressures on the walls.

Tani (8) also presents the results of an experimental investigation of flow separation related to a step or a groove. As Roshko, Tani found that the shear stress developed in the mixing or shear zone is balanced, primarily by pressure forces exerted on the solid surface of the slot. Additionally, the base pressure is essentially the same for different values of step height and boundary layer thickness and the pressure rise by flow reattachment increases as the step height is increased or the boundary layer thickness is reduced. It is Tani's viewpoint that the turbulent shear stress is necessarily set up in the mixing region in such a way that the forces acting on the fluid form a system of equilibrium, and that the most essential and intriguing part of the problem is concerned with the mixing process between the dissipative cavity flow and the non-dissipative main flow.

Seban, et al. (9), Seban and Fox (10), and Fox (1) presented measurements of surface pressure, recovery factors, and heat transfer coefficients on the bottom of two rectangular notches.

Here, the heat transfer coefficient was proportional to $(\rho_{\infty} u_{\infty})^{0.8}$, with the coefficient being greatest at the rear or downstream portion of the cavity. Fox (1) made additional measurements for a number of narrow notches having height to length ratios (h/b) from 4 to $4/7$ and again found the heat transfer coefficient to be proportional to $(\rho_{\infty} u_{\infty})^{0.8}$. Turbulent flow was ascertained in the notch region adjacent to the subsonic free stream, and vortex flow was observed within the cavity.

Concerning the analytical study of flow in a cavity, a number of distinctly different models are advanced. Chapman's model (11) treats the cavity as an isothermal low-velocity "dead-air" sink to which heat and momentum is transferred through the shear layer. In essence, it is a solution for an infinitely thick laminar shear layer with the boundary conditions at infinity represented by the conditions at the base of the slot. The shear layer is postulated to be the sole transfer-rate controlling mechanism disregarding the resistance between the inner wall and the fluid cavity. For laminar flow, these results compare very favorably with the experimental results of Larson (4).

Charwat (3) proposes a pulsating shear layer type model in which the fluid moves periodically in and out of the cavity, thus governing a transport of heat and momentum. Charwat's model depends on the unsteadiness of the flow at the exclusion of the other

mechanisms. The theory predicts the 0.6 power dependence of the heat transfer coefficient upon the mass velocity $\rho_{\infty} u_{\infty}$ that was measured by Larson in turbulent flow, and the corresponding 0.5 power in laminar flow. In this model, the cavity shape enters but incidentally with an allusion to a vortex located in the downstream corner.

Burggraf (12) however takes the cavity shape fully into account. In his model, Batchelor's (15) proposal of constant vorticity is assumed within the cavity. The vortex flow within the cavity is then coupled to the (laminar) external flow. However, for turbulent flow the velocity distribution along the separating streamline must be previously found by some other theory before this model can be utilized.

None of these analyses is adequate to explain the results in turbulent flow, particularly when the external flow is boundary layer in nature.

Thus, the present analytical and experimental study was undertaken and is aimed at delineating the turbulent momentum and heat transfer mechanism in the mixing zone of a cavity. A flow model of this zone is postulated on the basis of the well known concepts of mixing length and eddy diffusion yielding a rather satisfactory correlation with the experimental data.

2. EXPERIMENTAL STUDIES

2.1 Description of Test Equipment

A schematic diagram and photograph of the test rig employed for these tests are presented in Figures 1 and 2 respectively. The unit consists of a fan driven by a 3 horse-power variable speed motor, adjustable length flow channel, and a rectangular cavity. The channel was 2.5 in. wide and had an aspect ratio of 10 assuring substantially two-dimensional flow. The cavity width was varied from 1.0 to 2.5 inches and its depth was varied in 0.5 in. increments up to 4.5 inches. The flow channel (Figure 3) was varied in length from 13 to 29 inches, thus assuring a wide range of boundary layer thicknesses. The flow channel was connected to the fan by a second rectangular channel 3.5 in. wide x 21 in. high. Flow straighteners were placed within this ductwork approximately 85 inches upstream from the flow channel. The straighteners consisted of 3 inch long sections of 24 ga. sheet metal formed into a mesh having 1/2 in. squares. Turbulence screens were placed immediately upstream from the flow channel. These screens, which consisted of wire in various diameters and mesh sizes, effectively controlled the scale and intensity of the free stream turbulence.

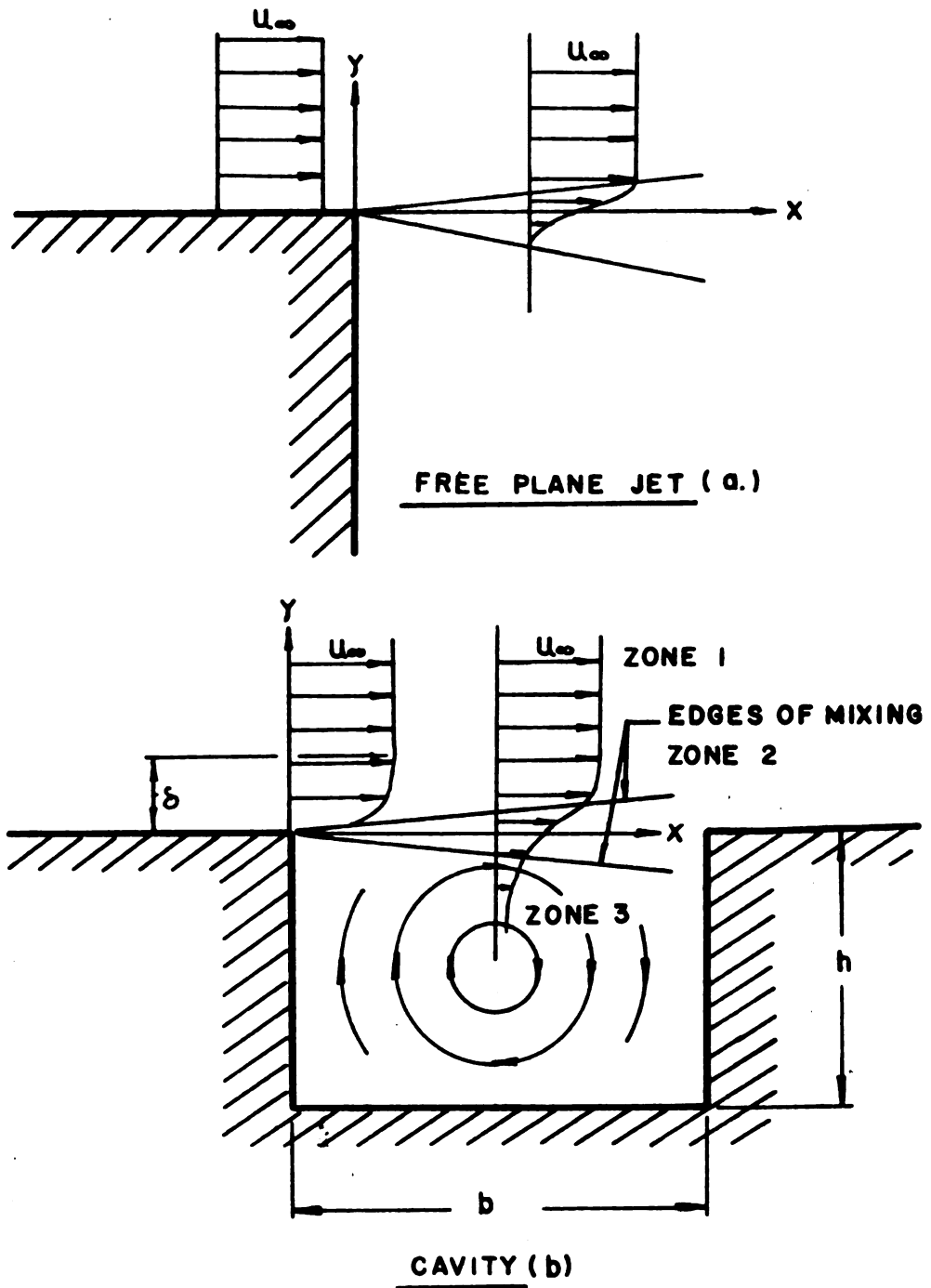


FIGURE 1
PHYSICAL FLOW MODEL

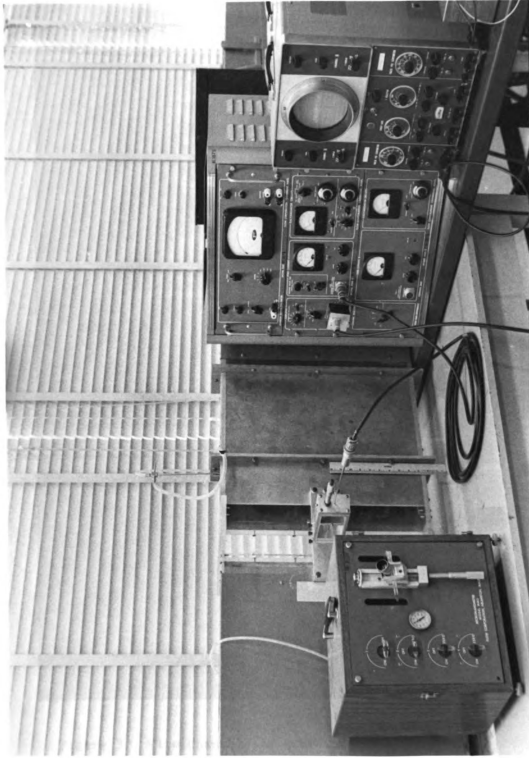


Figure 2. Test Rig

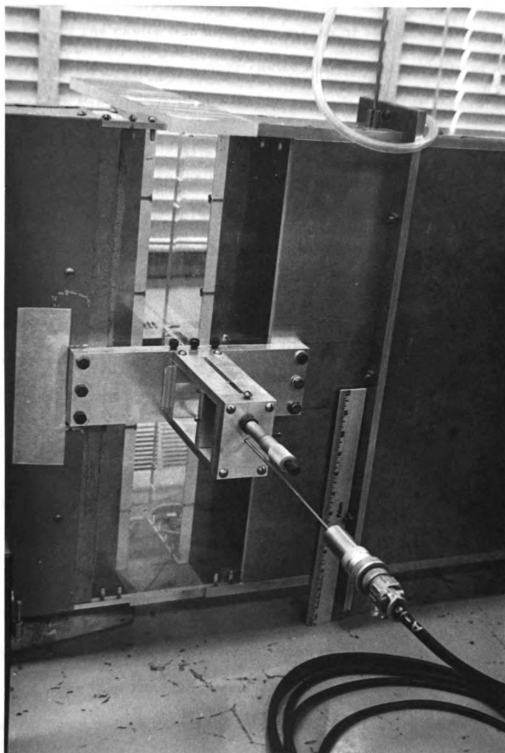


Figure 3. Flow Channel and Traversing Mechanism

The cavity was heated by means of electric Calrod heaters placed within the copper cavity walls. The quantity of heat required to keep the walls at constant temperature was measured by means of a watt meter (Model 432 by Weston Electrical Instrument Corporation), placed in the circuit of the heating rods. The heat losses were measured by two separate methods. First, thermocouples were buried within the cavity walls and the surrounding insulation. The heat losses were then estimated from local conduction losses. Radiation heat transfer was neglected due to the small temperature differences associated with the various tests. Secondly, the heat losses were measured directly for various wall temperatures using the wattmeter while the free stream velocity was held at zero. An estimate of the free convection losses within the cavity show them to be quite small ($\sim 5\%$) compared to the total heat loss. The two methods compare quite closely and remained within 8% for all tests.

Local heat transfer rates were also measured. To do this, a second cavity was employed (Figure 5) and which had 36 evenly spaced $0.005 \times 1/8$ inch series-connected nichrome ribbons. These ribbons were then attached over a 2 inch thick phenolic cavity. The heat rate was deduced from the measured power which was used to heat the cavity walls while the local temperature was measured with thermocouples attached to the underside of each ribbon. Further, the error in the temperature measurements was estimated to be within 0.4%.

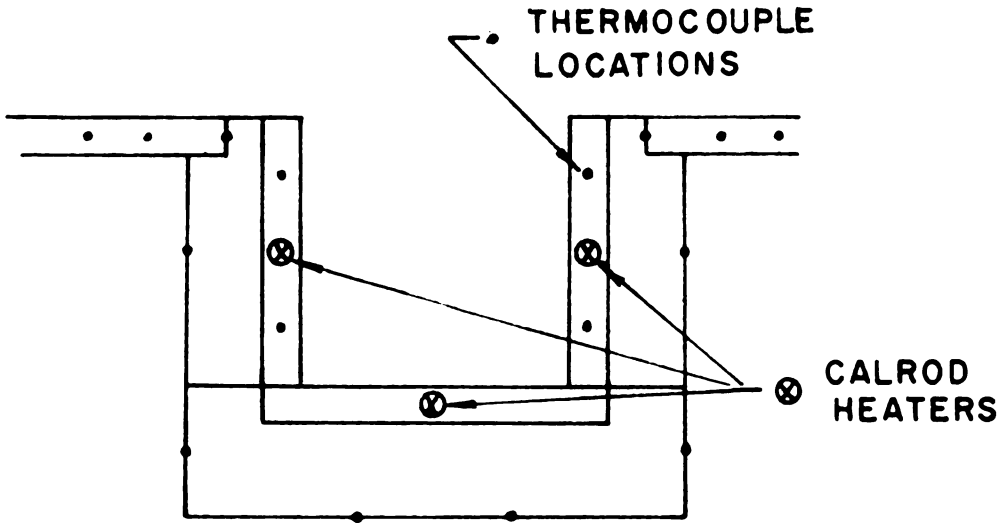
2.2 Instrumentation and Measurements

Shown in Figures 2 and 5 are the various instruments used in this study. The probes used for sensing velocity, turbulence, and temperatures were placed on a traverse mechanism that could be moved longitudinally, parallel to the mean flow, and transversely across the mixing region. A micrometer, accurate to ± 0.001 inches, was used for actuating the movement and measuring the transverse probe positions. The longitudinal probe positions were controlled by locating blocks as shown in Figure 3.

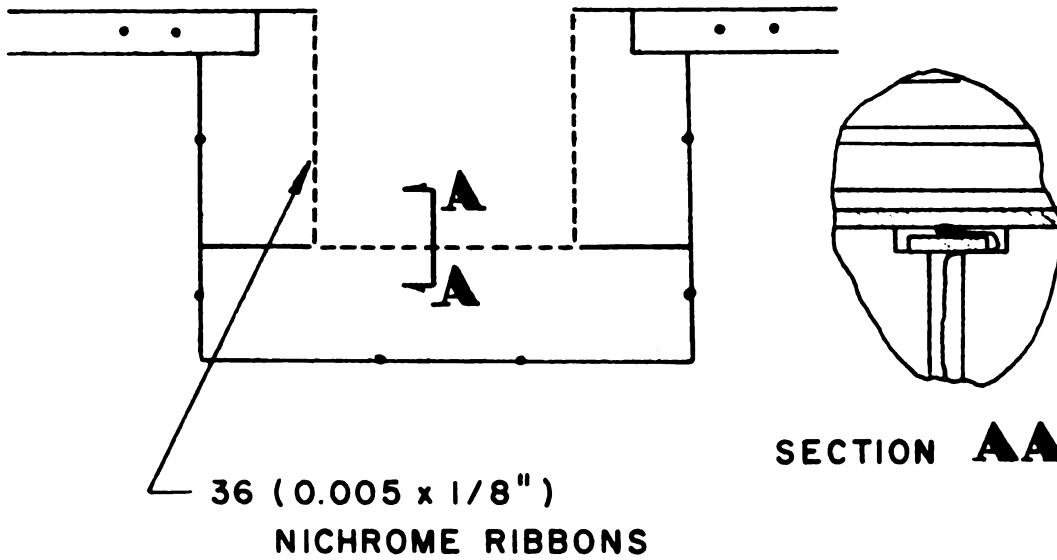
The temporal-mean velocity and the turbulent intensities were measured by means of a constant-current hot-wire anemometer (Model HWB ser. no. 216 by Flow Corporation, Arlington, Mass.), in accordance with the Flow Corporation hot-wire manual.

In measuring the turbulent shear, a single hot-wire probe was placed in two angular positions for each probe location. The turbulent shear was then calculated as described by Hinze (13).

Figure 2 shows the various instruments used in conjunction with the hot-wire anemometer. The signal from the hot-wire anemometer amplifier was fed through a 7KC low pass filter to a true-root-mean-square voltmeter (Model No. 320 by Ballantine Laboratories, Boonton, N. J.), using a response time of 2.5 seconds.



A. SCHEMATIC OF CAVITY USED FOR MEASURING AVERAGE HEAT TRANSFER RATES



B. SCHEMATIC OF CAVITY USED FOR MEASURING LOCAL HEAT TRANSFER RATES

FIGURE 4

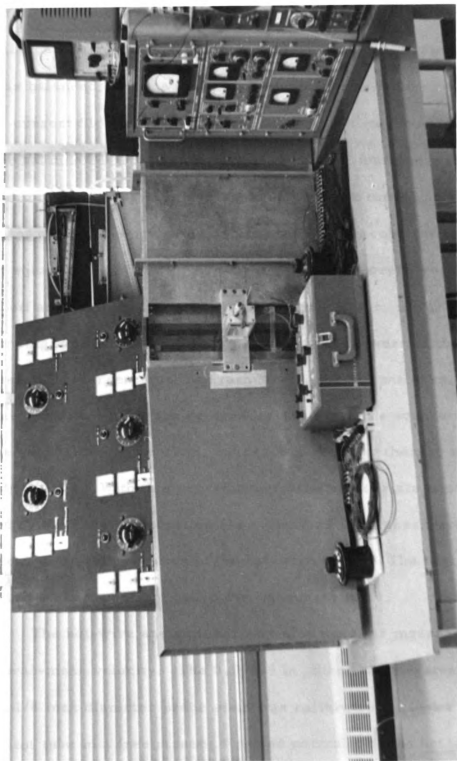


Figure 5. Test Rig

The general procedure used was first to balance the bridge cold, using the bridge null variable resistor. The value of the bridge balance was recorded and the current turned on. Again the bridge was balanced, and the value of the bridge balance was recorded. The wire current "I" was measured by means of the galvanometer and meter balance resistor and recorded in units of four times the current in milliamperes. The square wave was then turned on and the compensation frequency adjusted until the oscilloscope pattern was a perfect square wave. The square-wave and wire current were then switched off and the r. m. s. voltage measured. The r. m. s. value corresponding to this reading was M_n , which is a measure of the noise level. The current was then turned on again and the r. m. s. value again recorded using the designation $M_n + v$. The square wave was turned on again and the r. m. s. reading repeated thereby obtaining $M_n + v + s$. With this procedure and the appropriate equation suggested by the Flow Corporation (16), the turbulent measurements were repeated for each location of the hot-wire probe. The resistance ratio was kept constant at 1.6 throughout the tests.

The hot-wire anemometer was also used for measuring the temporal-mean velocity. The 0.00035 in. diameter tungsten hot-wire with 1/8 inch diameter probe stem was calibrated against a Prandtl pitot tube in a free stream directed normally to the hot wire and probe stem. For each filament used, a calibration curve I^2 vs $U^{1/2}$

was obtained. To obtain a velocity profile, the hot-wire was located at a number of positions and the filament currents recorded. From these known values of current at various locations the corresponding velocities were obtained through the most recent calibration curve for the particular filament in use. A typical calibration curve for the hot-wire anemometer probe is shown in Figure 6.

The air stream temperature was sensed by means of a copper-constantan (24 B ϕ S gauge) thermocouple located on the traverse mechanism. The EMF from the thermocouple was measured with a millivolt potentiometer (No. 8686 by Leeds and Northrup Corp. of Philadelphia, Pa.) with an expected error of $\pm 0.05\%$. The millivolts measured were then converted to temperature by means of tables available with the instrument. The thermocouple was first calibrated with an accurate mercury in glass thermometer.

The static pressure was sensed by static holes, 0.030 inches in diameter, drilled through the cavity walls, and was measured by means of a micromanometer (Model MM3 by Flow Corporation) which had n-butyl alcohol as its manometer fluid and a nominal accuracy of ± 0.0002 inches of manometer fluid. Since this manometer had a slow response, only temporal mean values of total head could be measured. Additionally, static pressure measurements were made within the shear layer ($y = 0$). In view of the uncertainty in the direction of flow within the shear layer, the accuracy of the static

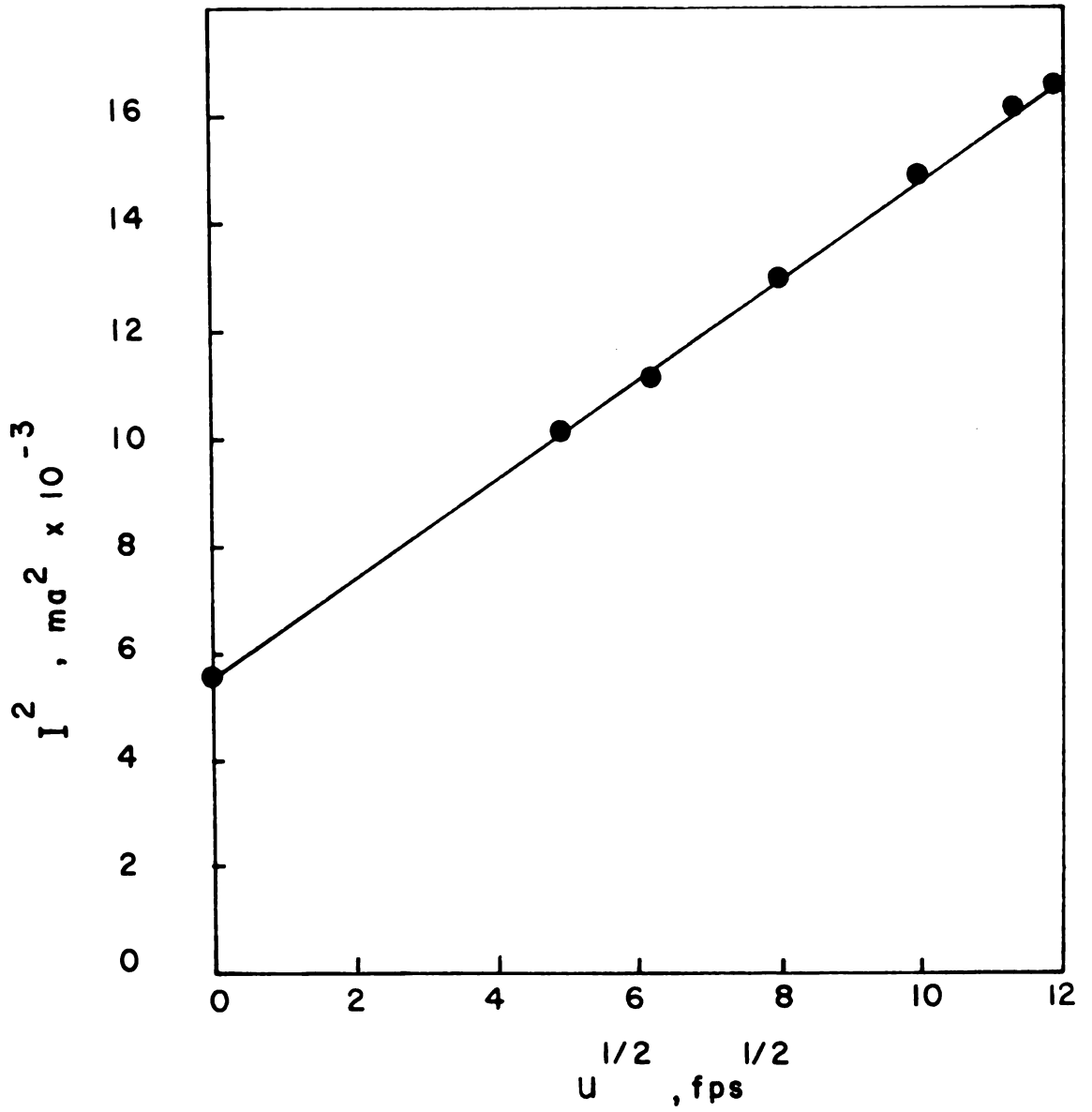


FIGURE 6
TYPICAL CALIBRATION CURVE
FOR THE HOT-WIRE ANEMOMETER

pressure distribution at $y = 0$ is questionable. But, since the flow is essentially two dimensional, the static pressure probe, held normally to the xy plane, is expected to yield reasonably accurate results. In an attempt to balance any flow component present which was normal to the xy plane, pressure distributions were taken with the static pressure tap held in both directions of the xy planes normal. The differences in pressure readings were negligible in this case and the associated measurements were considered satisfactory.

For flow visualization studies, it was found convenient to construct another cavity model. The model (shown in Figure 7) was subjected to flow of water approximately simulating the dynamic conditions in terms of the flow Reynolds number and the relative boundary layer thickness (δ/b). The streamlines were made visible by streaking aluminum powder over the water surface illuminated by light. Figures 16 and 17 represent the photographs of the flow patterns.

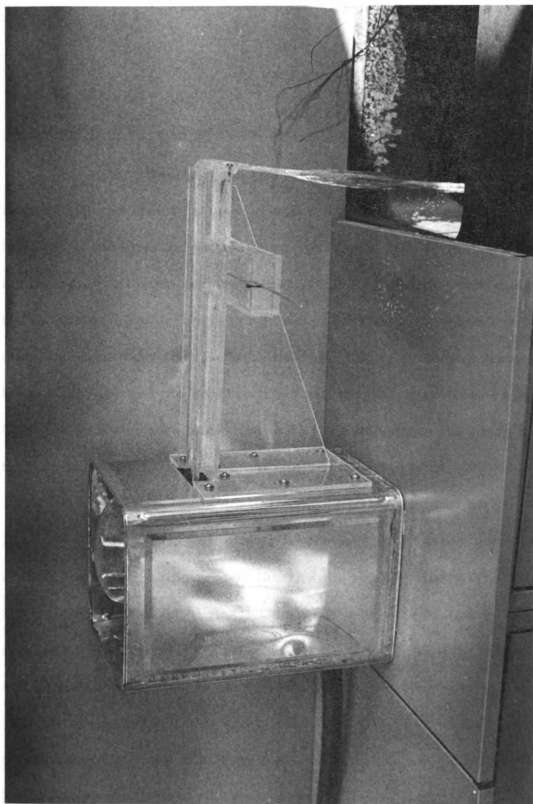


Figure 7. Water Flow Model

3. ANALYTICAL STUDIES

3.1 Analytical Flow Model

Many studies have been made of turbulent free plane jets, and in each case the flow was considered to consist of a uniform semi-infinite, plane-parallel jet issuing from a wall with a velocity of u_{∞} and merging with a motionless fluid (Figure 1). Under such conditions the oncoming fluid becomes completely turbulent within a very short distance from the wall. Because of this, turbulent mixing occurs between the jet and the surrounding fluid at rest. Particles of fluid from the surroundings are entrained by the jet so that the mass flow increases, while the total momentum remains constant.

Further, when dealing with such problems of turbulent jets it is assumed that this mixing is confined to a "shear zone," the width of this zone being proportional to the longitudinal distance from the point where the jet begins. Outside this zone, the flow is considered to be completely unaffected by the mixing process, while within the zone the flow is considered to be boundary layer in nature. That is, the solution being sought does not extend far in the transverse direction and only the transverse gradient of shear predominates. In our description of the cavity flow model, we have treated the shear

layer portion of the flow as a two-dimensional plane jet and accordingly applied the boundary layer equations of momentum and continuity. The turbulent shear stress and heat transfer terms are approximated by various phenomenological theories, e.g., mixing length, eddy diffusion, etc. With this, satisfactory solutions have been found.

3.2 Basic Equations

The equation of motion for a two dimensional flow can be written as:

$$\rho \left(\frac{\partial u}{\partial t} + u \frac{\partial u}{\partial x} + v \frac{\partial u}{\partial y} \right) = - \frac{\partial P}{\partial x} + \mu \left(\frac{\partial^2 u}{\partial x^2} + \frac{\partial^2 u}{\partial y^2} \right) \quad (3.1)$$

$$\rho \left(\frac{\partial v}{\partial t} + u \frac{\partial v}{\partial x} + v \frac{\partial v}{\partial y} \right) = - \frac{\partial P}{\partial y} + \mu \left(\frac{\partial^2 v}{\partial x^2} + \frac{\partial^2 v}{\partial y^2} \right) \quad (3.2)$$

Making estimates of the order of magnitude of the various terms, it is found that for a steady state turbulent flow in a boundary layer, Prandtl's approximation of Reynold's equation applies, namely:

$$\rho \left(\bar{u} \frac{\partial \bar{u}}{\partial x} + \bar{v} \frac{\partial \bar{u}}{\partial y} \right) = - \frac{dP}{dx} + \frac{\partial \tau}{\partial y} \quad (3.3)$$

and $\frac{\partial P}{\partial y} = 0$ (3.4)

where $\tau = \mu \frac{\partial \bar{u}}{\partial y} - \rho \overline{u'v'}$ (3.5)

and where the bars over the symbols indicate temporal mean values.

The equation of energy can be written as:

$$\rho C_p \left(\frac{\partial T}{\partial t} + u \frac{\partial T}{\partial x} + v \frac{\partial T}{\partial y} \right) = k \left(\frac{\partial^2 T}{\partial x^2} + \frac{\partial^2 T}{\partial y^2} \right) \quad (3.6)$$

which simplifies, with the same approximations as before to read as follows:

$$\bar{u} \frac{\partial \bar{T}}{\partial x} + \bar{v} \frac{\partial \bar{T}}{\partial y} = \frac{1}{\rho C_p} \frac{\partial Q}{\partial y} \quad (3.7)$$

where
$$Q = k \frac{\partial \bar{T}}{\partial y} - \rho C_p \overline{v'T'} \quad (3.8)$$

In addition to the equations of motion and energy, the equation of continuity must apply:

$$\frac{\partial(\rho \bar{u})}{\partial x} + \frac{\partial(\rho \bar{v})}{\partial y} = 0 \quad (3.9)$$

3.3 Solution of Momentum Equation

According to the experimental evidence (Figure 19), the pressure was found to remain relatively constant along a substantial portion of the shear layer. Thus, the pressure term in equation (3.3) is neglected, giving:

$$\bar{u} \frac{\partial \bar{u}}{\partial x} + \bar{v} \frac{\partial \bar{u}}{\partial y} = \frac{1}{\rho} \frac{\partial \tau}{\partial y} \quad (3.10)$$

Upon assuming constant density, the continuity equation becomes:

$$\frac{\partial \bar{u}}{\partial x} + \frac{\partial \bar{v}}{\partial y} = 0 \quad (3.11)$$

Boussinesq (17) suggested the coefficient ϵ_m (eddy diffusivity of momentum) for momentum transfer by turbulence. Using this theory, the turbulent shear stress may be expressed as:

$$\tau = \rho \epsilon_m \frac{\partial \bar{u}}{\partial y} \quad (3.12)$$

Assuming the turbulent effects are considerably larger than the molecular effects, equation (3.10) becomes:

$$\bar{u} \frac{\partial \bar{u}}{\partial x} + \bar{v} \frac{\partial \bar{u}}{\partial y} = \frac{1}{\rho} \frac{\partial}{\partial y} \left(\rho \epsilon_m \frac{\partial \bar{u}}{\partial y} \right) \quad (3.13)$$

The overall transfer of momentum from the cavity to the free stream takes place through a mixing region as depicted in Figure 1 (b). For the purpose of this analysis, the flow region over the cavity was divided into three different zones.

In the first zone [Figure 1 (b)] the flow remains unaffected by the mixing process within the shear layer. Thus, for the case of an oncoming turbulent boundary layer of thickness δ , the flow above the shear zone is assumed to obey the usual 1/7 power law.

Within the second zone, the shear stress term is postulated to obey the identical relationship as for the free plane jet as discussed by Abramovich (14). The shear zone is postulated to be symmetrical about $y = 0$ with its growth rate proportional to x . The equation used for the boundaries of this zone was $y = \pm 0.08829 x$. This value was chosen as it corresponds to the line which describes

the growth rate of a free plane jet. Also, the plot of $\overline{u'v'}/\bar{u}^2$ (Figure 8) is seen to justify this choice. Thus:

$$\tau = \rho \frac{a^3}{2} x^2 \frac{\partial \bar{u}}{\partial y} \left| \frac{\partial \bar{u}}{\partial y} \right| \quad (3.14)$$

where "a" is an empirical constant characterizing the structure of the flow of a jet. Its value for free jets is 0.09 (14). However, for the shear layer of the cavity a value of 0.12 yields a better correlation with the experimental data. The momentum eddy diffusivity is expressed by:

$$\epsilon_m = \frac{1}{2} a^3 x^2 \frac{\partial \bar{u}}{\partial y} \quad (3.15)$$

Then equation (3.13) becomes:

$$\bar{u} \frac{\partial \bar{u}}{\partial x} + \bar{v} \frac{\partial \bar{u}}{\partial y} = a^3 x^2 \frac{\partial \bar{u}}{\partial y} \frac{\partial^2 \bar{u}}{\partial y^2} \quad (3.16)$$

Choosing the coordinate system (x, η) as in the free jet case (14)

where:

$$\eta = \frac{y}{ax} \quad (3.17)$$

and letting the stream function

$$\psi = a u_\infty x f(\eta) \quad (3.18)$$

equation (3.16) becomes

$$f''' + f = 0 \quad (3.19)$$

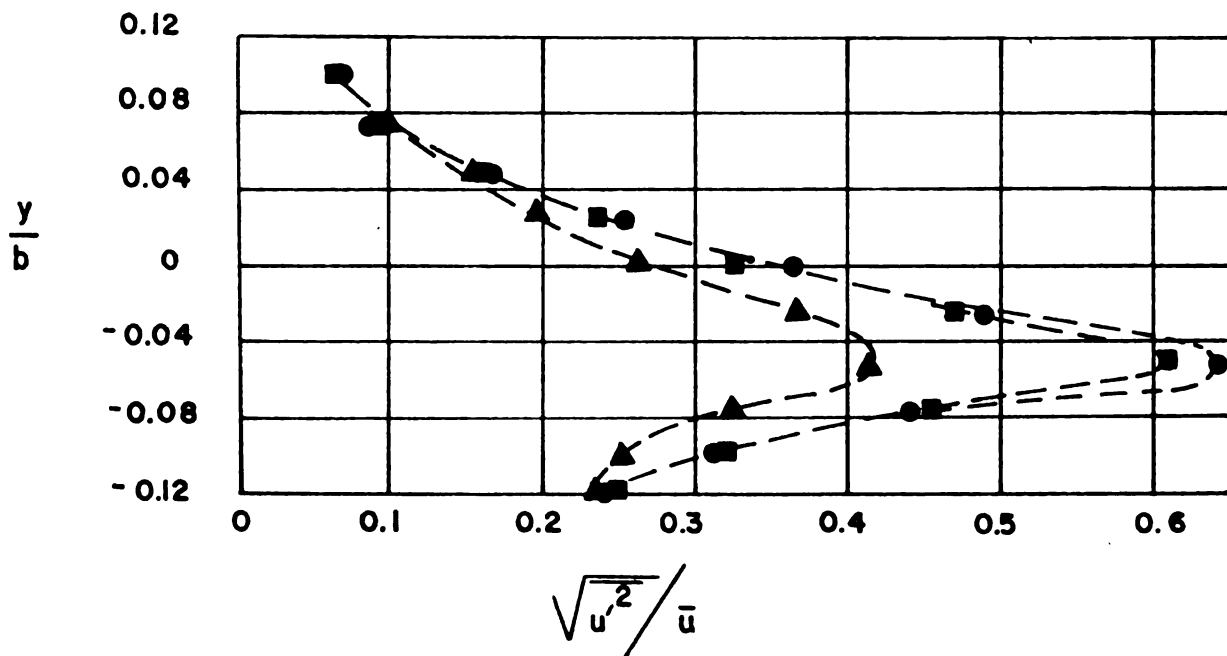
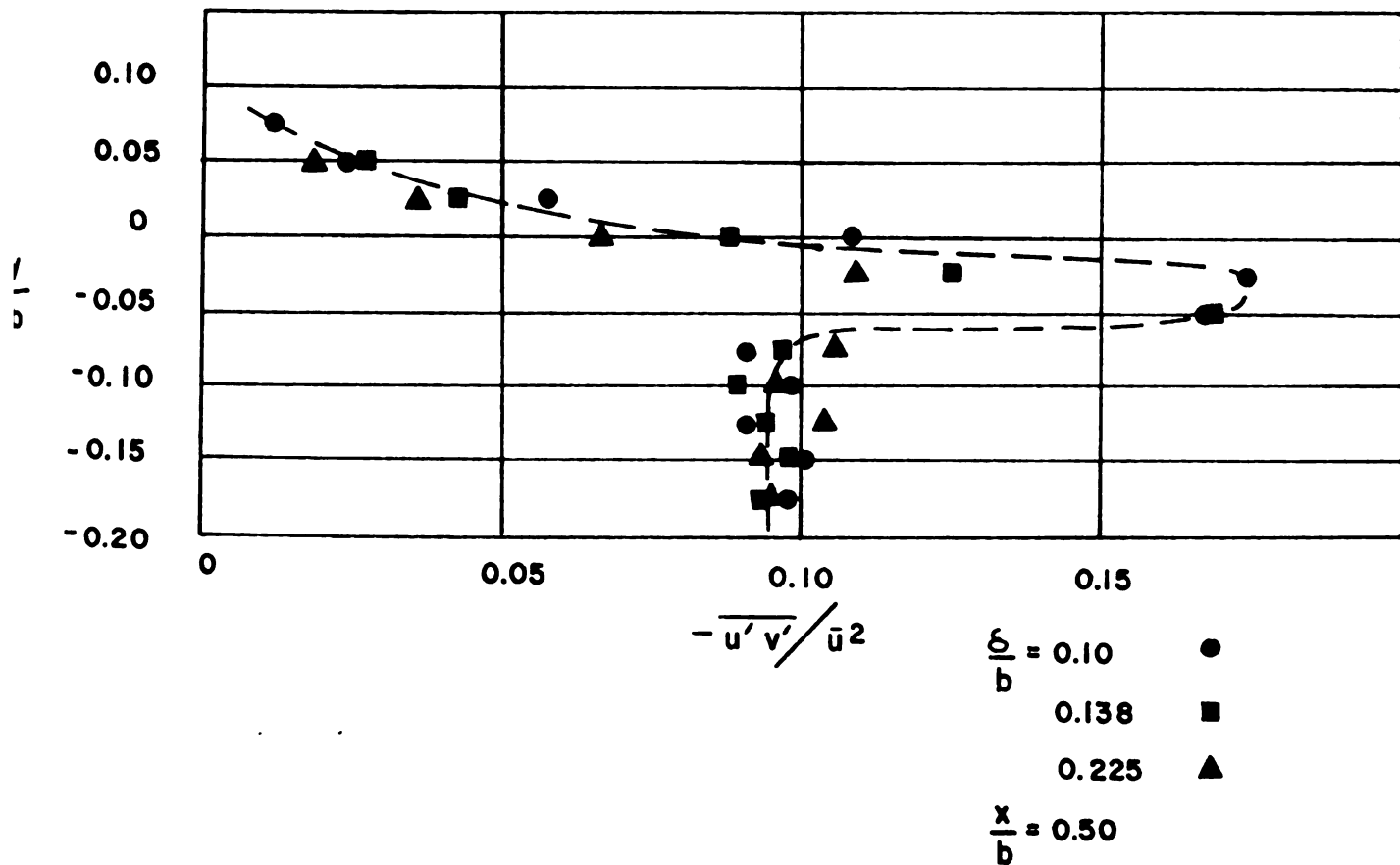


FIGURE 8
 A TYPICAL DISTRIBUTION OF THE QUANTITIES
 $\sqrt{u'^2}/\bar{u}$ AND $\overline{u'v'}/\bar{u}^2$
 ($h/b = 1.0$)

The solution of equation (3.19) is (14).

$$\frac{\bar{u}}{u_{\infty}} = f'(\eta) = k_1 e^{-\eta} + k_2 e^{\eta/2} \cos\left(\frac{\sqrt{3}}{2}\eta\right) + k_3 e^{\eta/2} \sin\left(\frac{\sqrt{3}}{2}\eta\right) \quad (3.20)$$

To evaluate the three constants k_1 , k_2 , and k_3 the boundary conditions utilized were:

1. The velocity is continuous from zone 1 to zone 2.
2. The velocity gradient is continuous from zone 1 to zone 2.
3. The turbulent shear stress has a maximum at $y = 0$.

The latter condition is justified by experimental evidence (see Figure 8 and Reference 1).

For a zero oncoming boundary layer thickness, the velocity in zone 1 is uniform. Thus, at the edge of zones 1 and 2 $f' = 1$ and $f'' = 0$. In this case, equation (3.20) becomes:

$$\frac{\bar{u}}{u_{\infty}} = 0.0684 e^{-\eta} + 0.79415 e^{\eta/2} \cos\left|\frac{\sqrt{3}}{2}\eta\right| + 0.28854 e^{\eta/2} \sin\left|\frac{\sqrt{3}}{2}\eta\right| \quad (3.21)$$

However, for a finite oncoming boundary layer thickness, the zone 1 velocity obeys the usual 1/7 power law. Boundary conditions 1 and 2 will then vary with x and the similarity of solutions implied by equation (3.19) no longer exists.

Proceeding with these varying boundary conditions, while acknowledging that the assumption of similarity must be violated somewhere, we obtained the following approximate but satisfactory solution.

$$\begin{aligned}
 k_1 &= 0.06840 g(x) + 1.1610 g'(x) \\
 k_2 &= 0.79415 g(x) - 0.47552 g'(x) \\
 k_3 &= 0.28854 g(x) + 0.71076 g'(x)
 \end{aligned}
 \tag{3.22}$$

Where, $g(x)$ denotes the local velocity ratio at the edge of zones 1 and 2 and $g'(x)$ its gradient.

For similarity to hold, the values of k_1 , k_2 , and k_3 must, of course, be constant. The extent of this violation is shown in Figure 9, where these k 's are plotted versus x/b .

Then, since $g(x)$ and $g'(x)$ come directly from the usual 1/7th power law, the entire solution may be expressed in terms of a constant term and the Reynolds number which describes the turbulent boundary layer thickness.

Finally, for the third zone the flow velocity and shear stress cannot be taken as zero as for the free plane jet. However, experimental evidence indicates that within this third zone the quantity

$\frac{\overline{u'v'}}{-2u}$ remains approximately uniform (independent of y).

Thus, $\frac{\overline{u'v'}}{-2u} = \text{constant}$.

Then, since $\tau \sim \overline{u'v'}$ (bar indicates time-averaged quantity)

we have $\tau \sim u^{-2}$

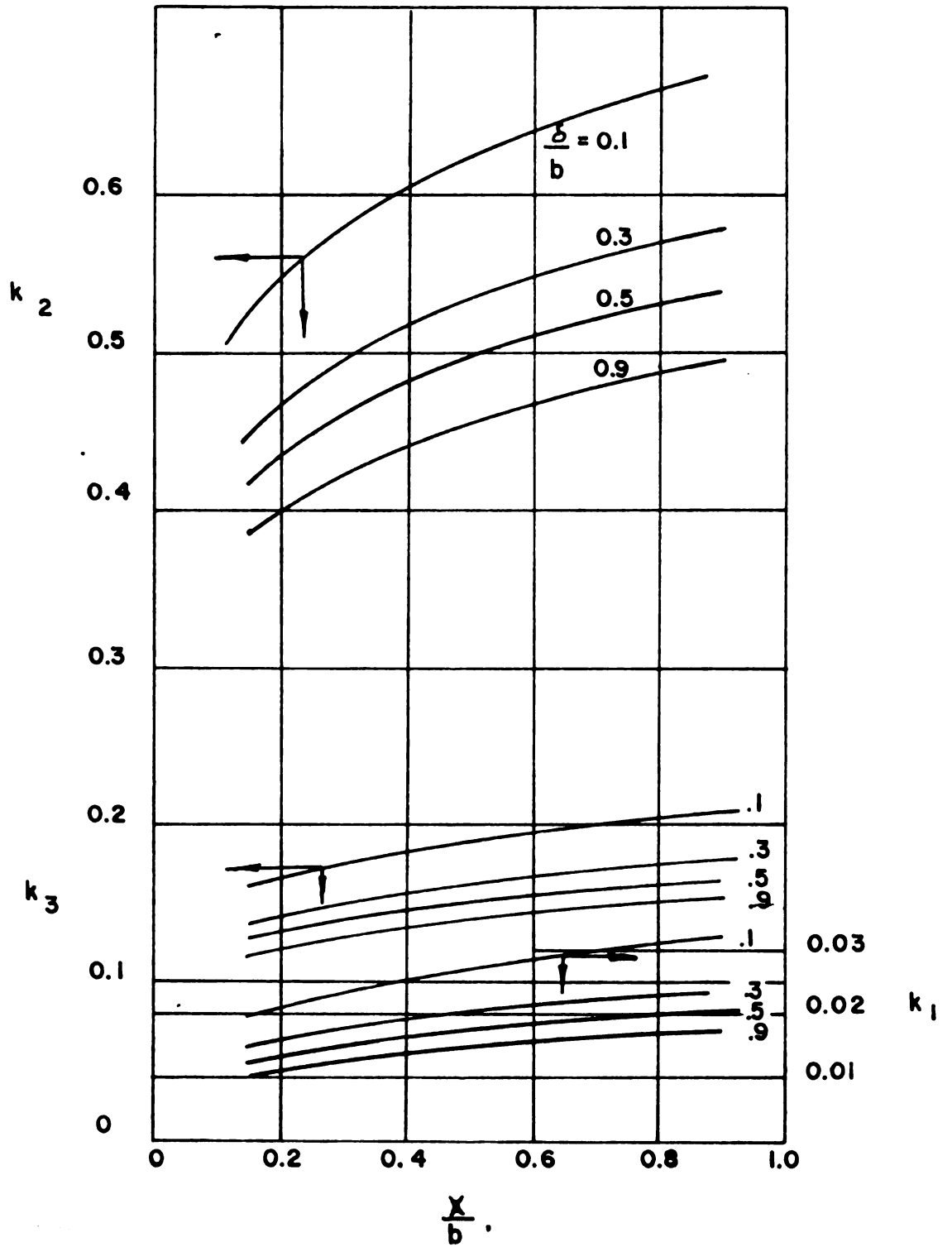


FIGURE 9
 CONSTANTS $k_1, k_2,$ & k_3 OF EQUATION (3.22)

Hence we write $\tau = \frac{1}{2} \rho k \bar{u}^{-2}$, where $k = \text{constant}$, and the expression for the eddy diffusivity in this zone is

$$\epsilon_m = \frac{1}{2} k \bar{u}^{-2} / \left(\frac{\partial \bar{u}}{\partial y} \right) \quad (3.23)$$

Equation (3.13), applied to this zone becomes:

$$\bar{u} \frac{\partial \bar{u}}{\partial x} + \bar{v} \frac{\partial \bar{u}}{\partial y} = k \bar{u} \frac{\partial \bar{u}}{\partial y} \quad (3.24)$$

Again letting

$$\psi = k u_{\infty} x F(\phi) \quad (3.25)$$

where $\phi = \frac{y}{kx}$ we obtain,

$$F'(\phi) + F(\phi) = 0 \quad (3.26)$$

with the solution as:

$$F(\phi) = C_1 e^{-\phi} = C_1 e^{-C_2 \eta} \quad (3.27)$$

where as before:

$$\eta = \frac{y}{ax} \quad (3.28)$$

The boundary conditions employed here for obtaining C_1 and C_2 were:

1. The velocity is continuous from zone 2 to zone 3.
2. The velocity gradient is continuous from zone 2 to zone 3.

The velocities in this zone are readily calculated from

$$\frac{\bar{u}}{u_{\infty}} = F'(\phi) = -C_1 e^{-C_2 \eta} \quad (3.29)$$

Typical values for C_1 and C_2 are shown in Figure 10.

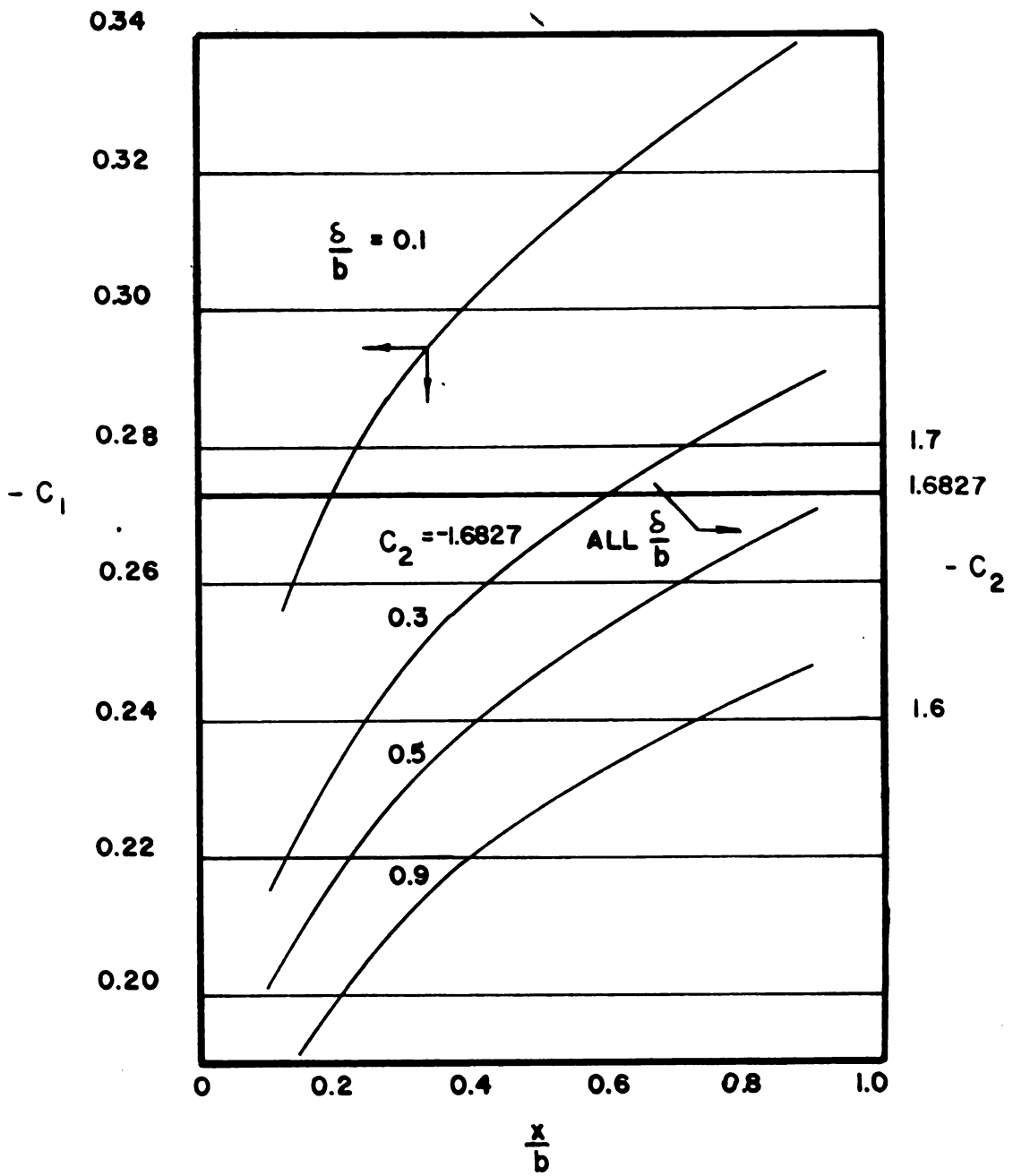


FIGURE 10
CONSTANTS C_1 AND C_2 OF EQUATION (3.29)

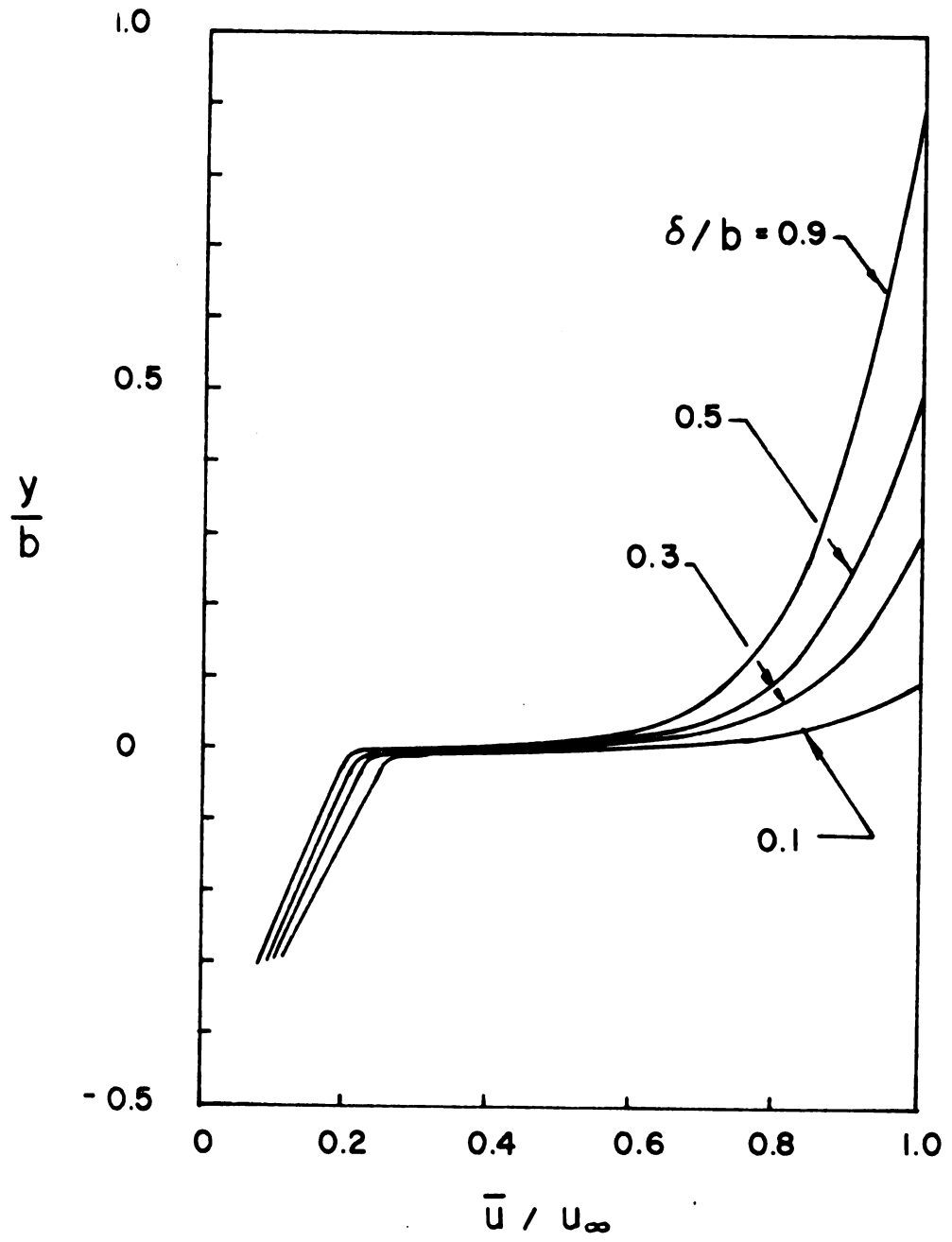


FIGURE II
VELOCITY DISTRIBUTION FOR $x/b = 0.15$

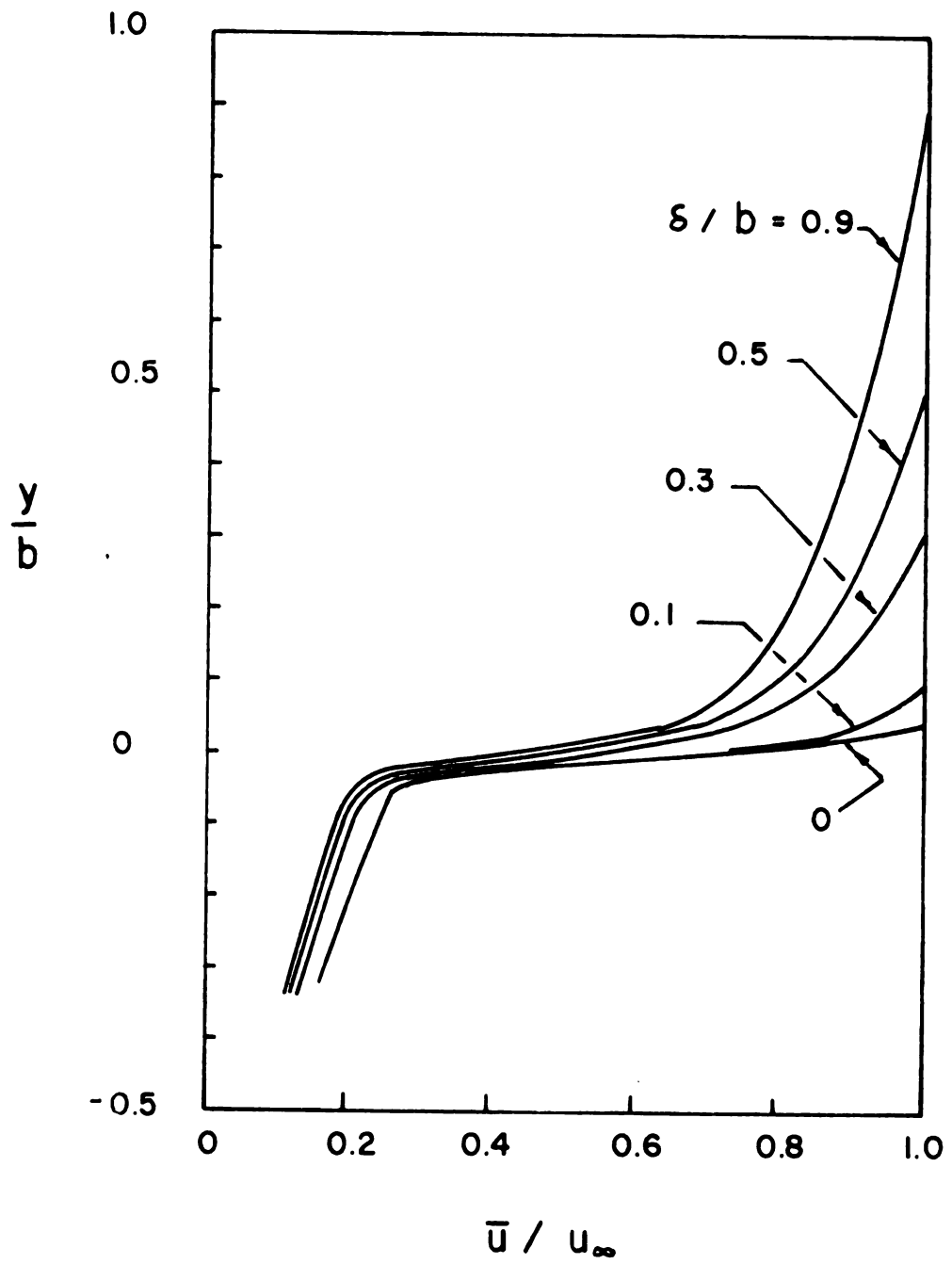


FIGURE 12
VELOCITY DISTRIBUTIONS FOR $x/b = 0.50$

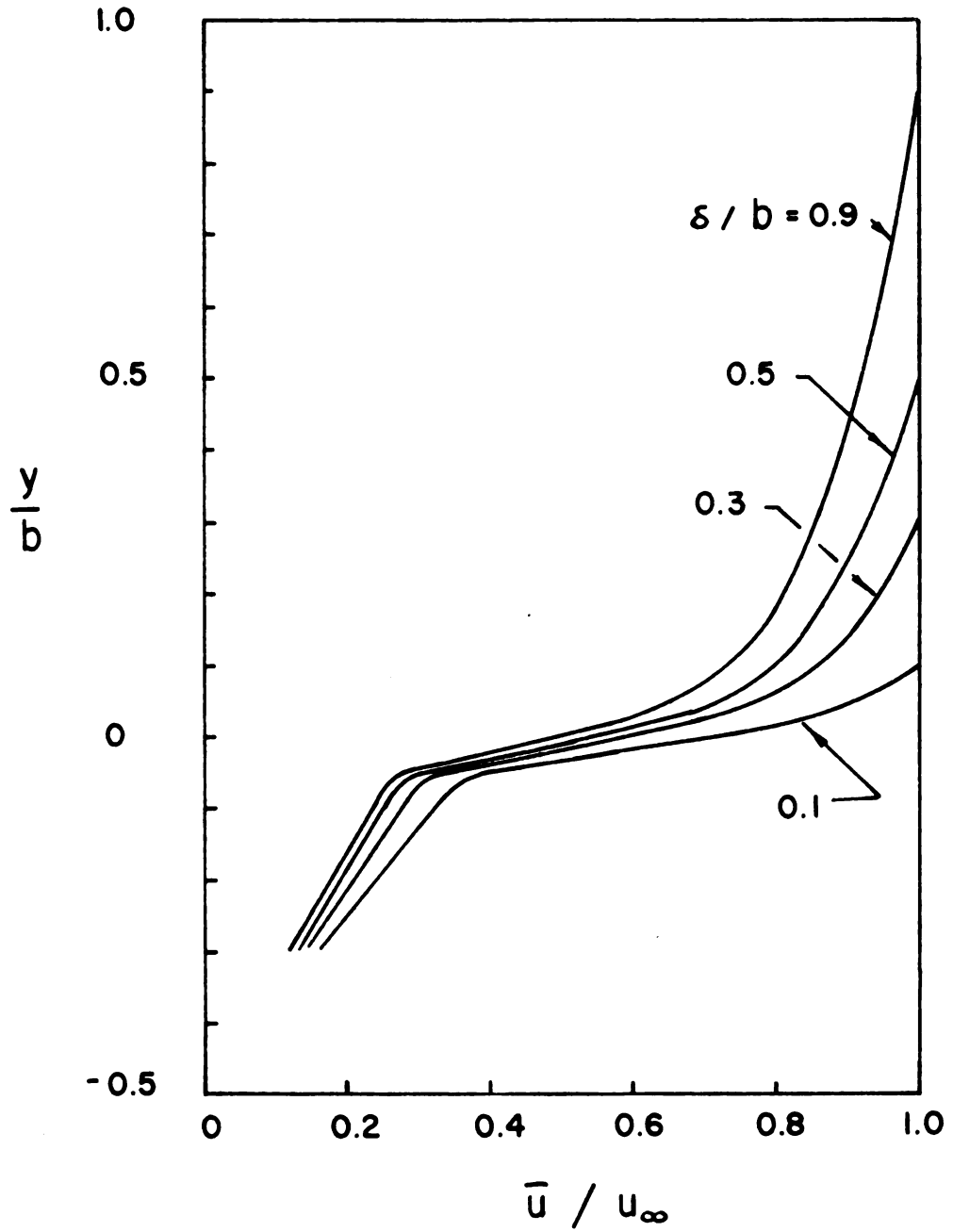


FIGURE 13
VELOCITY DISTRIBUTIONS FOR $x/b = 0.85$

It must be noted that at the edge of zone 2 and 3, the velocity and its gradient are forced to be continuous by choice of an appropriate number of constants, whereas the assumed shear distribution [in view of equations (3.15) and (3.23)] is discontinuous.

3.4 Solution of Energy Equation

Similarly, the energy equation becomes:

$$\bar{u} \frac{\partial \bar{T}}{\partial x} + \bar{v} \frac{\partial \bar{T}}{\partial y} = \frac{\partial}{\partial y} \left(\epsilon_h \frac{\partial \bar{T}}{\partial y} \right) \quad (3.30)$$

where $\epsilon_h = \frac{\overline{-v'T'}}{(\partial \bar{T} / \partial y)}$ = eddy diffusivity of heat.

Assuming the turbulent Prandtl number to be constant, $\frac{1}{C}$.

$$\text{Pr}_t = \frac{\epsilon_m}{\epsilon_h} = \frac{1}{C}$$

Then, for the shear zone:

$$\epsilon_h = \text{Ca}^3 x^2 \frac{\partial \bar{u}}{\partial y} \quad (3.31)$$

Equation (3.30), applied to this zone, becomes

$$\bar{u} \frac{\partial \bar{T}}{\partial x} + \bar{v} \frac{\partial \bar{T}}{\partial y} = \text{Ca}^3 x^2 \left(\frac{\partial \bar{u}}{\partial y} \frac{\partial^2 \bar{T}}{\partial y^2} + \frac{\partial \bar{T}}{\partial y} \frac{\partial^2 \bar{u}}{\partial y^2} \right) \quad (3.32)$$

Measured temperature distributions within the cavity (Figures 26-31) show that the temperature gradient is very large across the shear zone. But, outside this zone and within the inviscid

core, the temperature remains uniform. For deeper cavities, the temperature increases again for locations deeper than $y/b = -1$, thus again indicating secondary vortices.

Burggraf has shown similar behavior, with a nearly constant temperature over the inviscid core. Although his analysis does not consider secondary vortices, his results for predicting this core temperature agree quite well with experiment. Burggraf gives:

$$\frac{T_o - T_\infty}{T_w - T_\infty} = \frac{1}{\sqrt{(1 + \frac{b}{h}) A}} \quad (3.33)$$

where, for laminar flow $A = 2$ and T_o is the average core temperature. With this temperature, we are now in a position to solve the energy equation (3.32).

let
$$\theta = \frac{\bar{T} - T_\infty}{T_o - T_\infty}$$

and
$$\eta = \frac{y}{ax}$$

assuming $\theta = \theta(\eta)$

equation (3.32) becomes:

$$C f'' \theta'' + C \theta' f''' + f \theta' = 0 \quad (3.34)$$

But, from the momentum equation we have:

$$f''' + f = 0 \quad (3.35)$$

Therefore,

$$C f'''' \theta' + C f'' \theta''' - f'''' \theta' = 0 \quad (3.36)$$

$$\frac{\theta'''}{\theta'} = \frac{1-C}{C} \frac{f''''}{f''} \quad (3.37)$$

Integrating

$$\theta' = K (f'')^{\frac{1-C}{C}} \quad (3.38)$$

Where K is an arbitrary constant.

Similarly, for the third zone the energy equation becomes:

$$\bar{u} \frac{\partial \bar{T}}{\partial x} + \bar{v} \frac{\partial \bar{T}}{\partial y} = \frac{\partial}{\partial y} \left(\epsilon_h \frac{\partial \bar{T}}{\partial y} \right) \quad (3.39)$$

Once again assuming $\epsilon_h = C \epsilon_m$, we obtain for the third zone,

$$\epsilon_h = \frac{C k \bar{u}^{-2}}{2 \frac{\partial \bar{u}}{\partial y}} \quad (3.40)$$

$$\text{Thus, } \bar{u} \frac{\partial \bar{T}}{\partial x} + \bar{v} \frac{\partial \bar{T}}{\partial y} = \frac{\partial}{\partial y} \left(\frac{C k \bar{u}^{-2}}{2} \frac{\partial \bar{T} / \partial y}{\partial \bar{u} / \partial y} \right) \quad (3.41)$$

$$\text{Again, let } \theta = \frac{\bar{T} - T_\infty}{T_o - T_\infty} \quad (3.42)$$

$$\text{and, } \phi = \frac{y}{k x} \quad (3.43)$$

Equation (3.41) reduces to:

$$-f \theta' = \frac{C}{2} \frac{d}{d\phi} \frac{f'^2 \theta'}{f''} \quad (3.44)$$

However, from the momentum analysis, we have:

$$f' = -f \quad (3.45)$$

Thus, (3.44) becomes:

$$f' \theta' = -\frac{C}{2} \frac{d}{d\phi} (f' \theta') \quad (3.46)$$

$$\text{Integrating } f' \theta' = B_0 e^{\frac{-2\phi}{C}} \quad (3.47)$$

But, from equation (3.29)

$$f' = C_1 e^{-\phi} \quad (3.48)$$

$$\text{Therefore, } \theta' = B_1 e^{\frac{C-2}{C} \phi} \quad (3.49)$$

Integrating, and combining constants yields

$$\theta(\eta) = B_2 e^{B_3 \eta} + B_4 \quad (3.50)$$

where B_2 and B_4 are arbitrary constants, while

$$B_3 = \frac{C-2}{C} C_2 = 0.72116$$

Equation (3.38) was now integrated numerically, giving values for $\theta(\eta)$ over the shear zone. These values were then used to calculate the constants B_2 and B_4 , with the assumption that $\theta(\eta)$ and its gradient $\theta'(\eta)$ are continuous through zones 2 and 3. The constant K was next readjusted from initial "guesses" so as to

satisfy equation (3.33). Based upon best agreement with experimental results, the constant C was taken to be 1.4. For this value $\mathcal{K} \approx 0.5$ for all x/b and δ/b although it increases slightly with increasing x/b and decreases with increasing δ/b . Representative values of \mathcal{K} are plotted in Figure 15.

The total heat flux was given as:

$$q = \epsilon_h \rho C_p \frac{\partial \bar{T}}{\partial y} \quad (3.51)$$

or

$$q = C \epsilon_m \rho C_p \frac{T_o - T_\infty}{a x} \frac{d\theta}{d\eta}$$

Substituting for ϵ_m and $\frac{d\theta}{d\eta}$ for zone 2 gives:

$$q = C a \rho u_\infty (T_o - T_\infty) \mathcal{K} [f''(\eta)]^{1/C} \quad (3.52)$$

or at $\eta = 0$ where

$$f''(\eta=0) = \frac{k_1}{2} + \frac{\sqrt{3}}{2} k_2 + k_3$$

and

$$q = C a \rho C_p u_\infty (T_o - T_\infty) \mathcal{K} \left(\frac{k_1}{2} + \frac{\sqrt{3}}{2} k_2 + k_3 \right)^{1/C} \quad (3.53)$$

Defining an average heat flux as:

$$\bar{q} = \int_{\frac{x}{b}=0}^1 q d\left(\frac{x}{b}\right) = a \rho C_p C u_\infty (T_o - T_\infty) \int_0^1 \mathcal{K} \left(\frac{k_1}{2} + \frac{\sqrt{3}}{2} k_2 + k_3 \right)^{1/C} d\left(\frac{x}{b}\right) \quad (3.54)$$

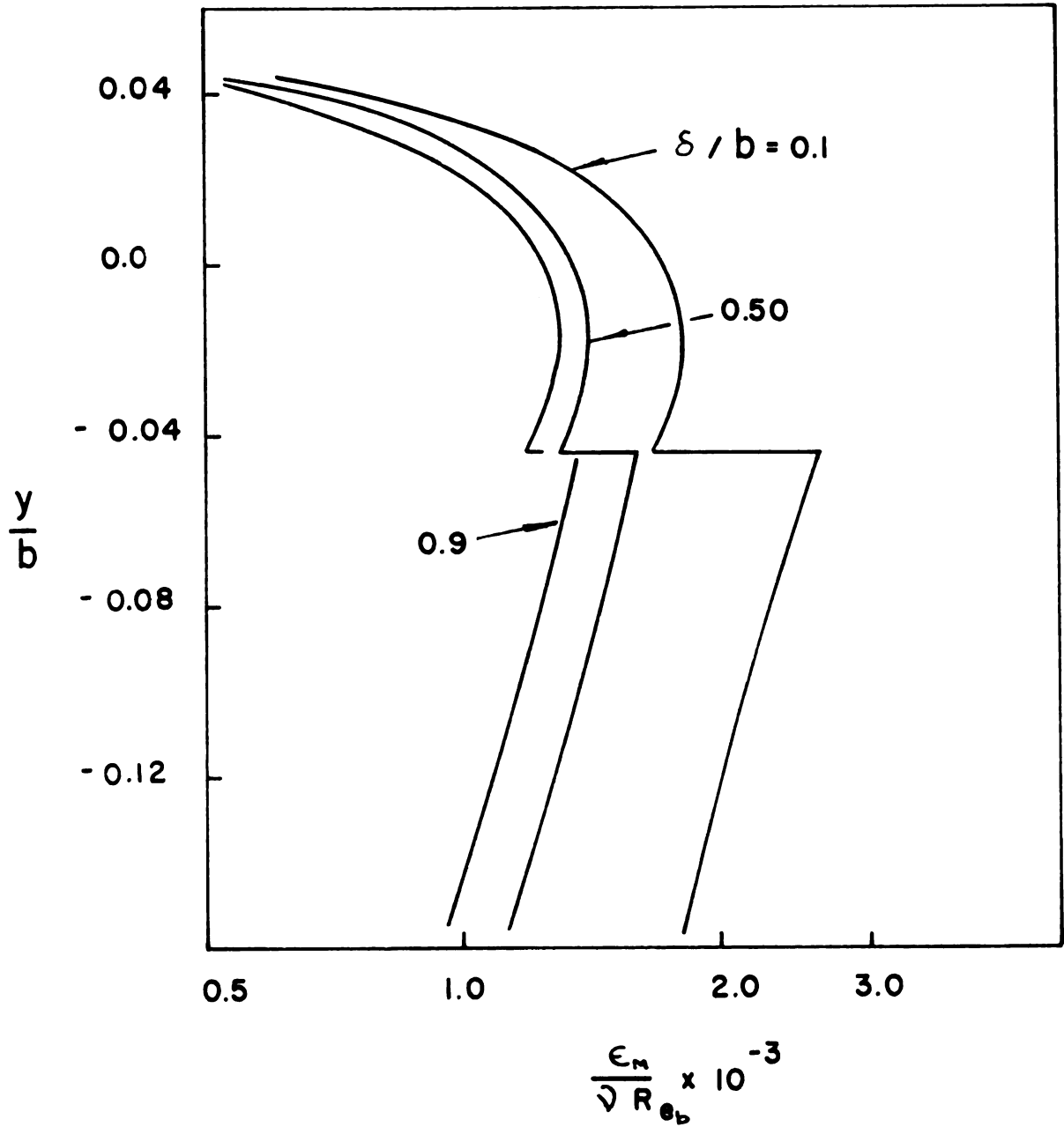


FIGURE 14
 TYPICAL DISTRIBUTION OF ϵ_M FOR
 $x/b = 0.50$

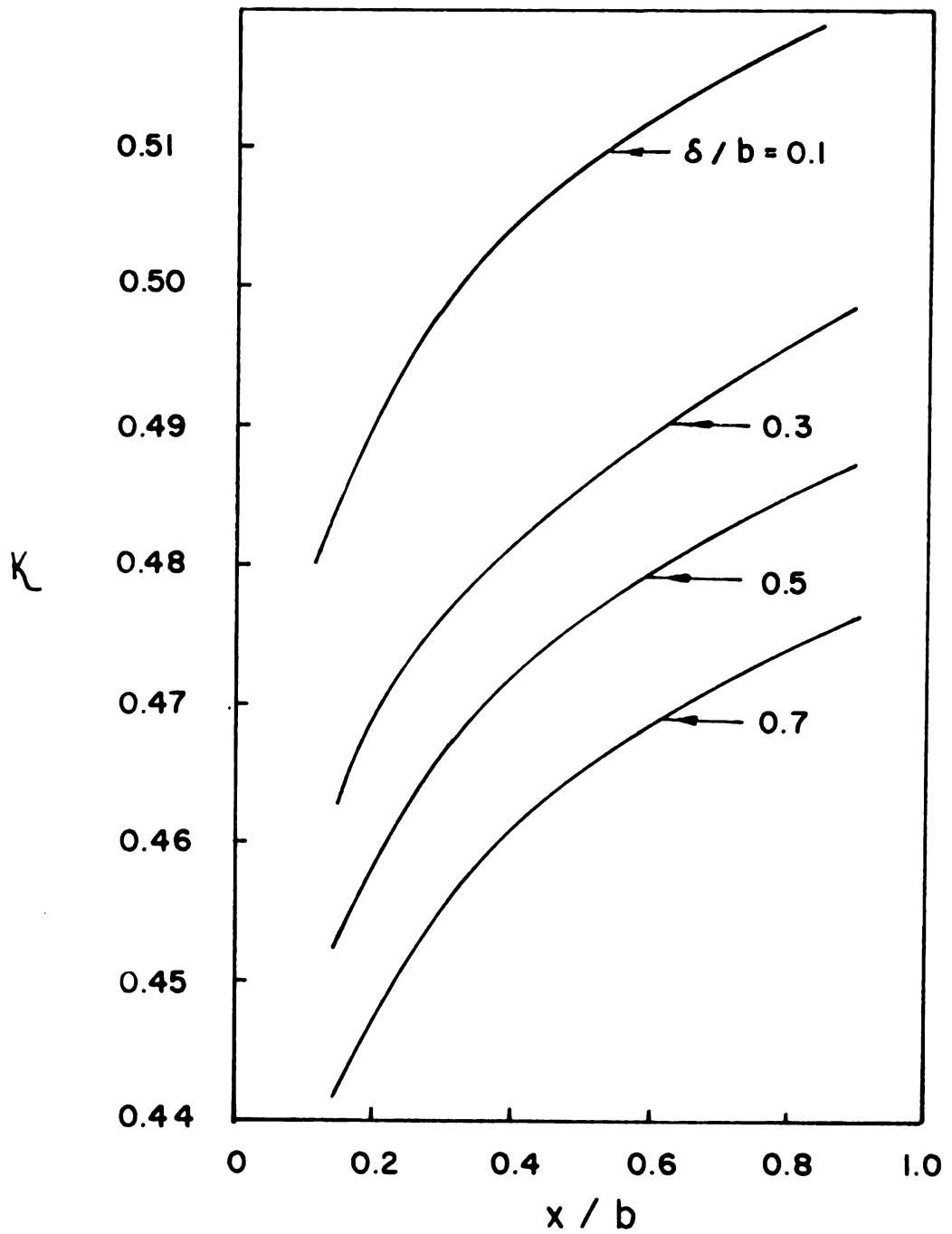


FIGURE 15

FACTOR K OF EQUATION (3.38)

The average Stanton number becomes:

$$\overline{St} = \frac{\overline{q}}{\rho C_p u_\infty (T_o - T_\infty)} = Ca \zeta \quad (3.55)$$

where

$$\zeta = \int_0^1 K \left(\frac{k_1}{2} + \frac{\sqrt{3}}{2} k_2 + k_3 \right)^{1/C} d \left(\frac{x}{b} \right) \quad (3.56)$$

It should also be noted that the Stanton number, as defined in equation (3.55), is independent of cavity depth and follows the equation:

$$\overline{St} = 0.0365 \left(\frac{\delta}{b} \right)^{-0.1367} \quad (3.57)$$

If however the heat transfer is desired in terms of the more conventional $(T_w - T_\infty)$, equation (3.33) may be used. Defining

$$\overline{St} = \frac{\overline{q}}{\rho C_p u_\infty (T_w - T_\infty)} \quad (3.58)$$

Then,

$$\overline{St} = \frac{Ca \zeta}{\sqrt{A \left(1 + \frac{b}{h} \right)}} \quad (3.59)$$

4. ANALYTICAL AND EXPERIMENTAL RESULTS

4.1 Flow Patterns

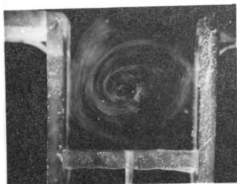
The flow patterns portrayed in Figures 16 and 17 reveal interesting effects of the height to width ratio of the slot on the structure of the vortices inside the cavity. For $h/b = 1$, there is a single vortex and it is stable, resembling almost a solid-body rotation. Around h/b of 1.75 there appear secondary vortices in transition and at a value of $h/b = 2$ one observes a rather well-defined double-vortex structure (presumably stable). Transition again seems to take place around $h/b = 2.5$ when the number of vortices oscillates between two and three. Finally, for h/b of approximately 3, we see three cells with vortices stacked on top of each other. The vortices were observed in a state of counter-rotation to each other.

4.2 Pressure

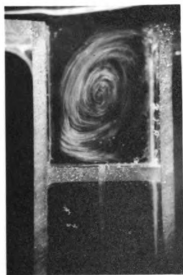
Pressure is represented for the notch surfaces as a pressure coefficient C_p that is defined by

$$C_p = \frac{P - P_\infty}{\frac{1}{2} \rho_\infty u_\infty^2}$$

where P_∞ is the reference surface pressure which was measured



$h/b = 1.0$

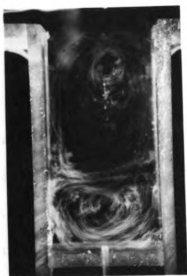


$h/b = 1.5$



$h/b = 1.75$

FIGURE 16
PICTURES OF CAVITY FLOW PATTERNS



$h/b = 2.0$



$h/b = 2.5$



$h/b = 3.0$

FIGURE 17
PICTURES OF CAVITY FLOW PATTERNS

0.25 inches ahead of the cavity. ρ_{∞} is the density as given for air at the free stream temperature and pressure.

Figures 18 and 19 represent the measured pressure distribution along the cavity walls and along the shear layer. As pointed out by Roshko (7), lower pressures near the center of the walls and bottom and high pressures at the corners are typical of a single, stable vortex. Near the top surface of the downstream edge, the pressure suddenly rises. This rather abrupt change is apparently caused by the boundary layer separating at the front edge and impinging on the downstream wall. It is noteworthy that the pressure distribution at the walls is rather sensitive to changes in depth. Also, the tendency to form a single vortex in the cavity with $h/b = 1$ is seemingly unaffected by the state of the boundary layer ahead of the cavity. However, the pressures and forces due to the flow do indeed depend on the state of the boundary layer.

The pressure distribution longitudinally along the shear layer evidently remains uniform except near the recompression corner. As remarked before, use was made of this fact in neglecting the pressure gradient in the momentum equation. Roshko (7) has shown the shear stress acting on the cavity walls to be of two orders of magnitude lower than the pressure coefficients and the pressure-drag coefficient. The difference between the integrated mean-value of C_p over the upstream and downstream walls, and made dimensionless by the dynamic pressure $\frac{1}{2} \rho u_{\infty}^2$, is plotted in Figure 20.

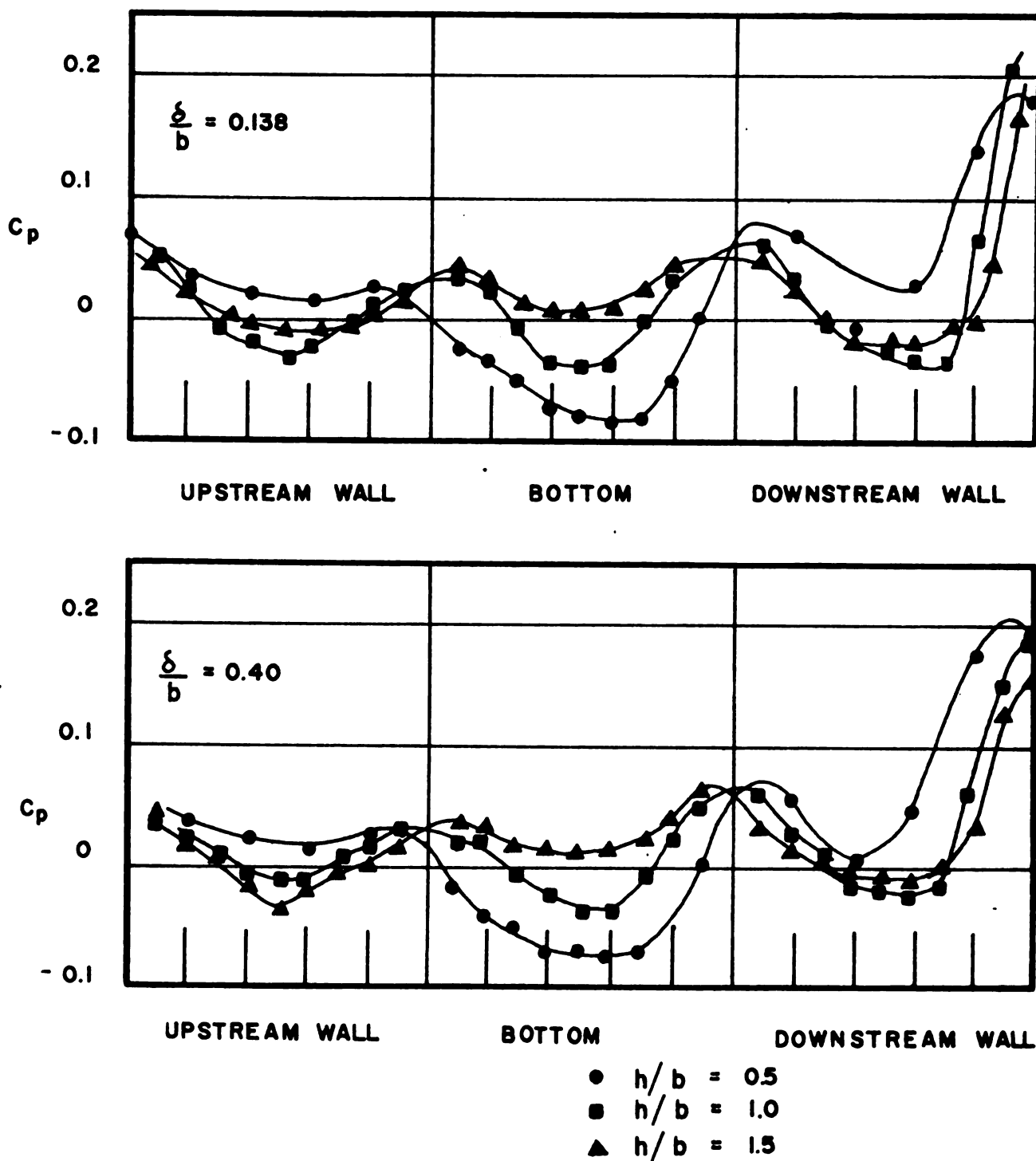


FIGURE 18
 MEASURED PRESSURE DISTRIBUTION ALONG CAVITY
 WALL SHOWING INFLUENCES OF HEIGHT TO WIDTH RATIO

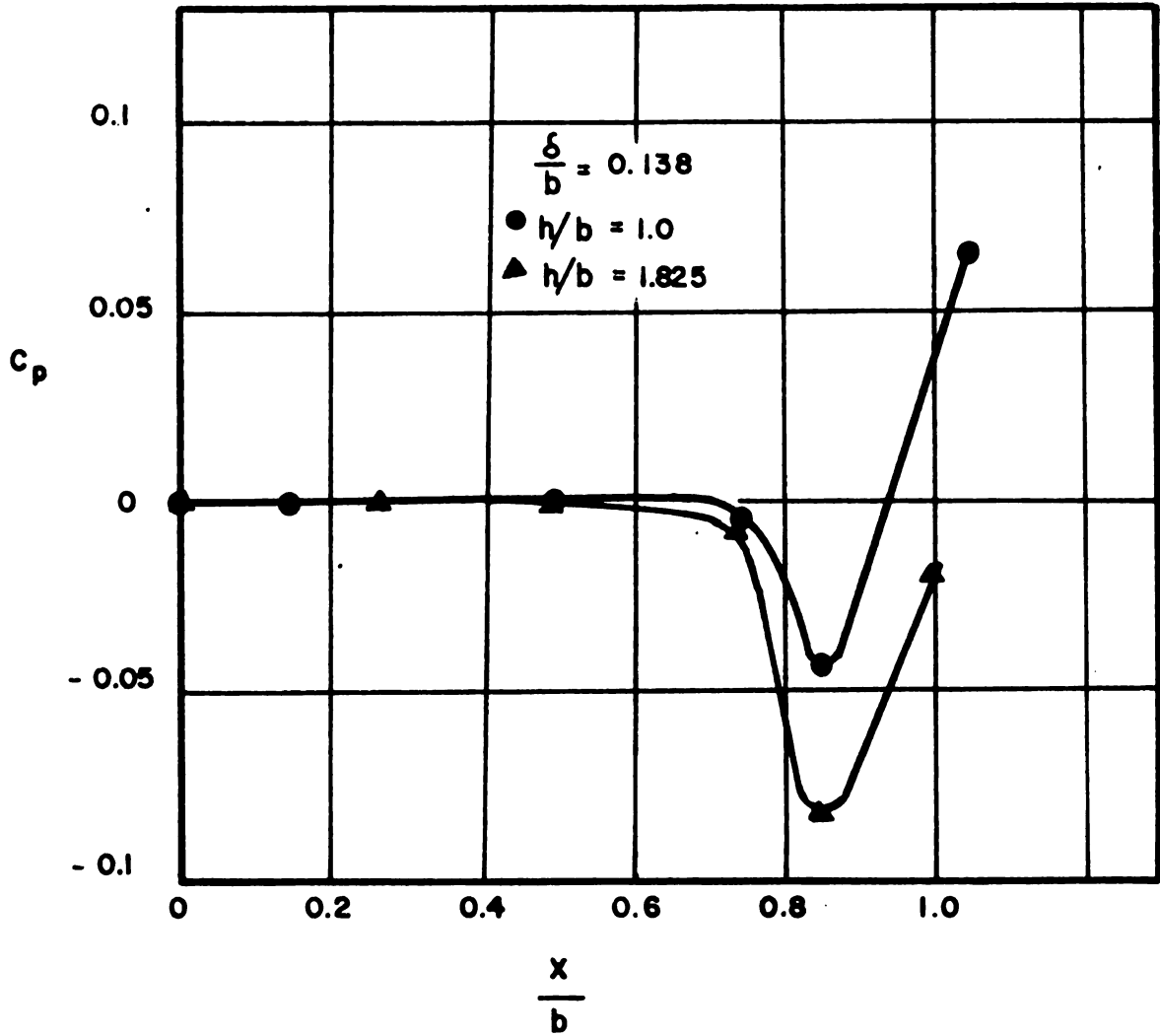


FIGURE 19
TYPICAL LONGITUDINAL PRESSURE DISTRIBUTION
IN THE SHEAR LAYER (at $y=0$)

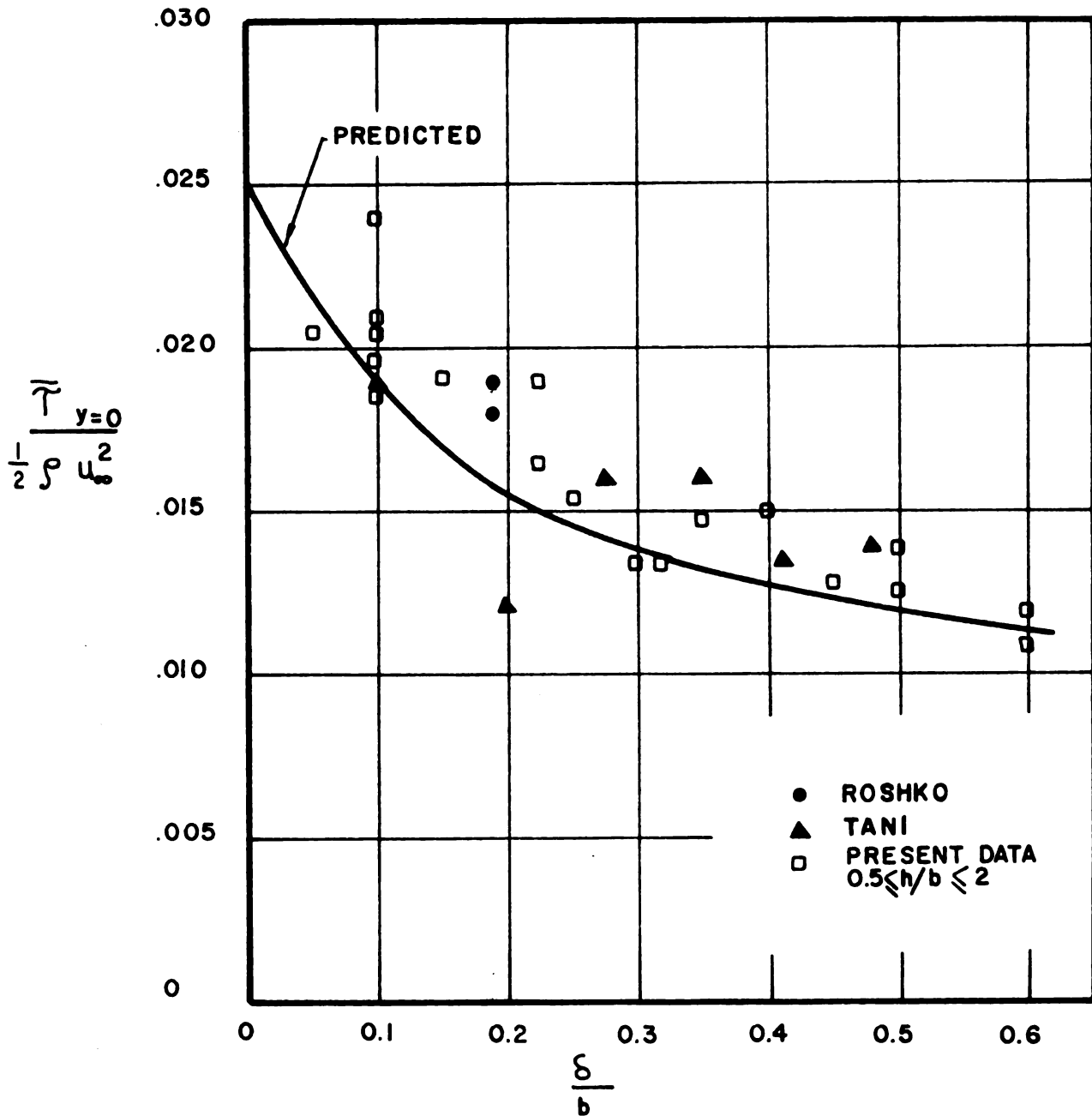


FIGURE 20
 PREDICTED EFFECT OF THE ONCOMING BOUNDARY
 LAYER THICKNESS ON THE TURBULENT SHEAR
 STRESS AND COMPARISON WITH EXPERIMENT

The cavity flow is maintained chiefly by the turbulent shear stress which is set up within the mixing region. Thus, the turbulent shear stress developed in the mixing or shear zone is balanced, primarily by the pressure forces exerted on the cavity walls. The comparison is made between this measured value and the integrated average shear stress (at the mean dividing streamline, i. e., $y = 0$) from the analysis. It is clear that the influence of the relative oncoming boundary layer thickness (δ/b) is quite substantial on the drag due to the slot. The data points are for different h/b values ranging between 0.5 and 2.0.

4.3 Velocity

- The velocity data are presented in a form of a ratio of the local velocity to the free-stream velocity measured at mid-channel immediately upstream of the cavity. The ratio is presented as \bar{u} / u_{∞} where no attempt is made to correct for temperature effects, because of the small temperature differences.

In Figures 21, 22, and 23 the data from the velocity measurements are compared with the results of the equation:

$$\begin{aligned} \frac{\bar{u}}{u_{\infty}} = & [0.06840 g(x) + 1.1610 g'(x)] e^{-\eta} \\ & + [0.79415 g(x) - 0.47552 g'(x)] \cos\left(\frac{\sqrt{3}}{2} \eta\right) e^{\eta/2} \\ & + [0.28854 g(x) + 0.71076 g'(x)] \sin\left(\frac{\sqrt{3}}{2} \eta\right) e^{\eta/2} \end{aligned} \quad (4.1)$$

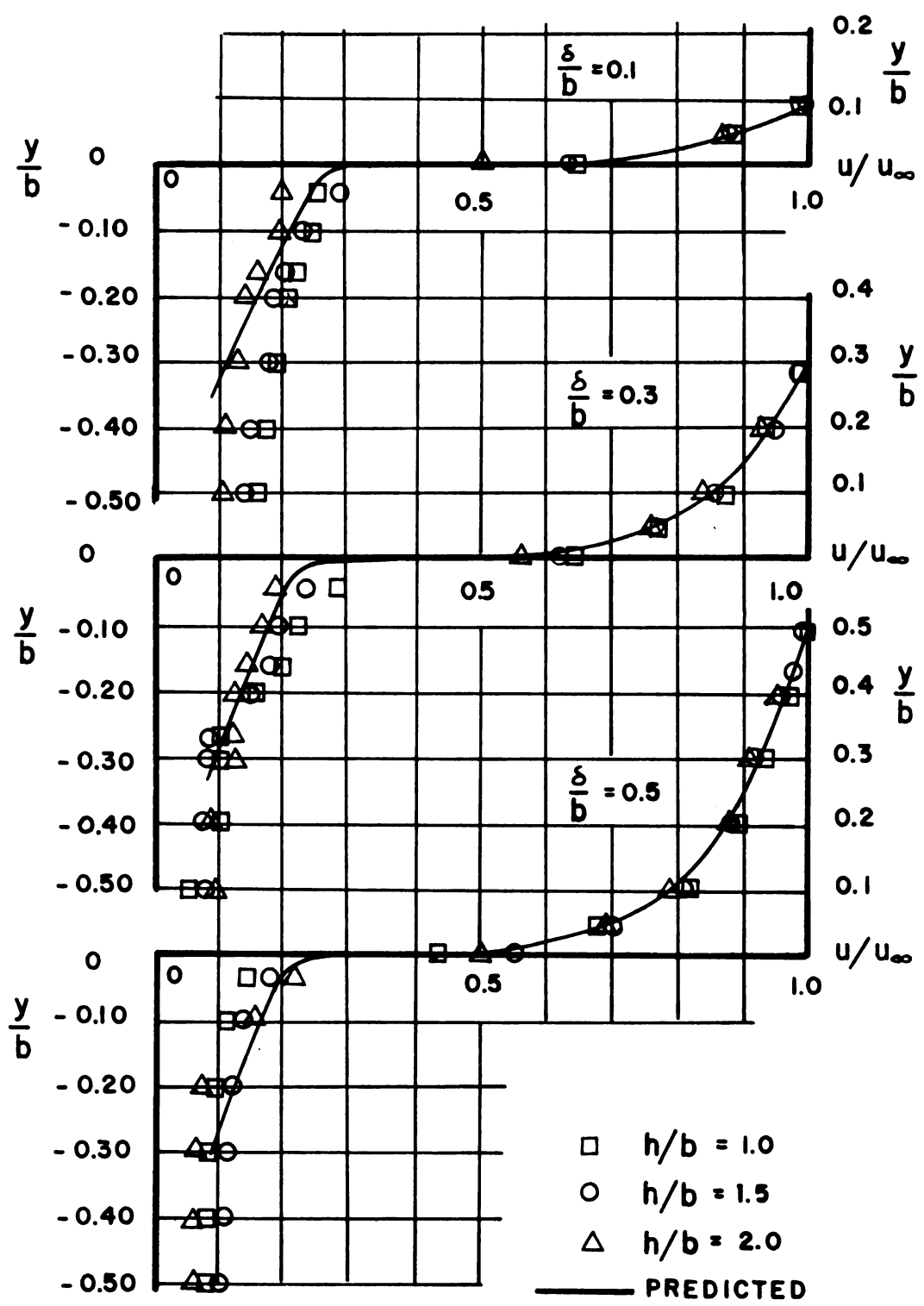


FIGURE 21
COMPARISON OF EXPERIMENTAL AND
ANALYTICAL VELOCITY PROFILES ($x/b = 0.15$)

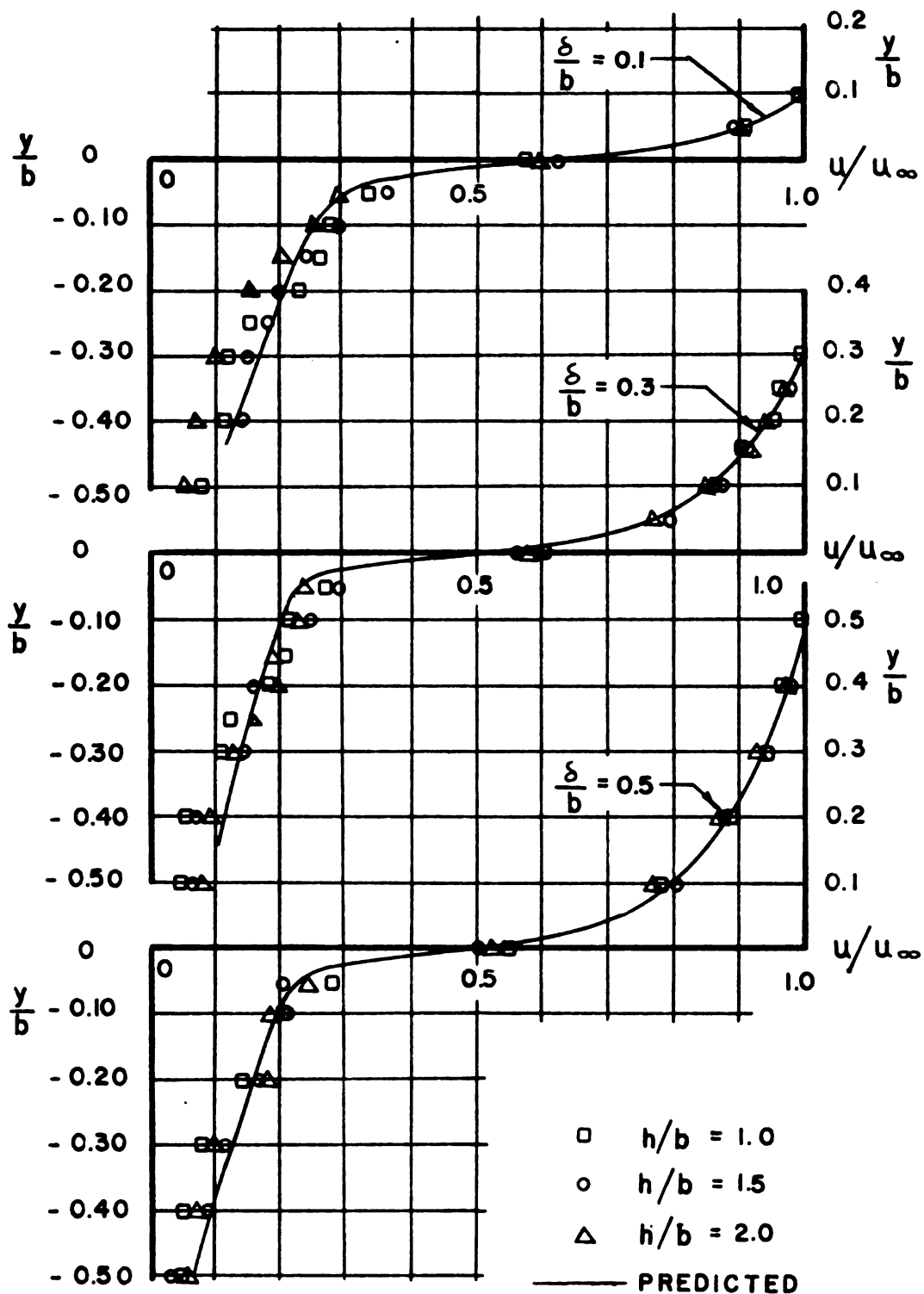


FIGURE 22
COMPARISON OF EXPERIMENTAL AND
ANALYTICAL VELOCITY PROFILES ($x/b = 0.50$)

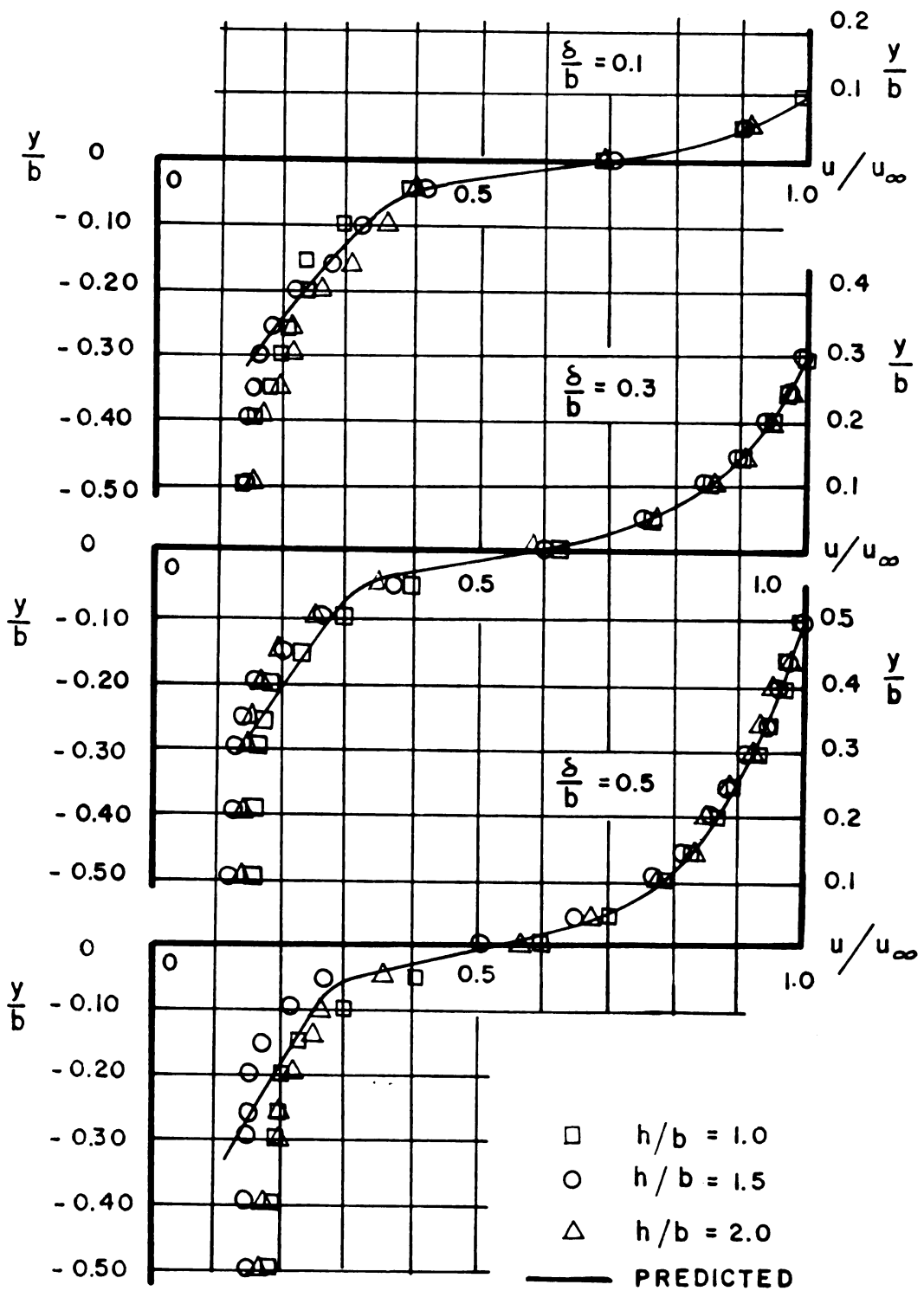


FIGURE 23
 COMPARISON OF EXPERIMENTAL AND
 ANALYTICAL VELOCITY PROFILES ($x/b = 0.85$)

This function contains the constant "a" which was chosen to be 0.12. Velocity profiles from the tests, each at three distances from the cavity origin ($x/b = .15, .50, \text{ and } .85$), are presented as data points in Figures 21, 22, and 23. The solid line represents equation (4.1). This line is seen to correlate the data reasonably well. Furthermore, streamlines calculated from these equations are shown in Figure 24, and again appear to be reasonable when compared with the observed pattern of Figure 16.

4.4 Turbulence

Figure 25 shows the transverse distributions of the turbulent intensity and the shear stress as measured by the hot-wire anemometer. The solid line in Figure 25 (b) represents the theoretical shear stress and is seen to correlate the experimental data adequately. From the figure it is quite apparent that both the local shear stress and the turbulence are maximum at a point coinciding with the dividing streamline ($y = 0$); and they are quite sensitive to changes in the relative thickness of the approaching boundary layer (δ/b).

In Figure 8, transverse distributions of the quantities $-\overline{u'v'}/\bar{u}^2$ and $\sqrt{\overline{u'^2}/\bar{u}}$ are shown. The relative size of the turbulent boundary layer once more appears to have significant effects on the latter quantity whereas the former $\overline{u'v'}/\bar{u}^2$ remains relatively unaffected. It must also be noted that the quantity $\overline{u'v'}/\bar{u}^2$ remains

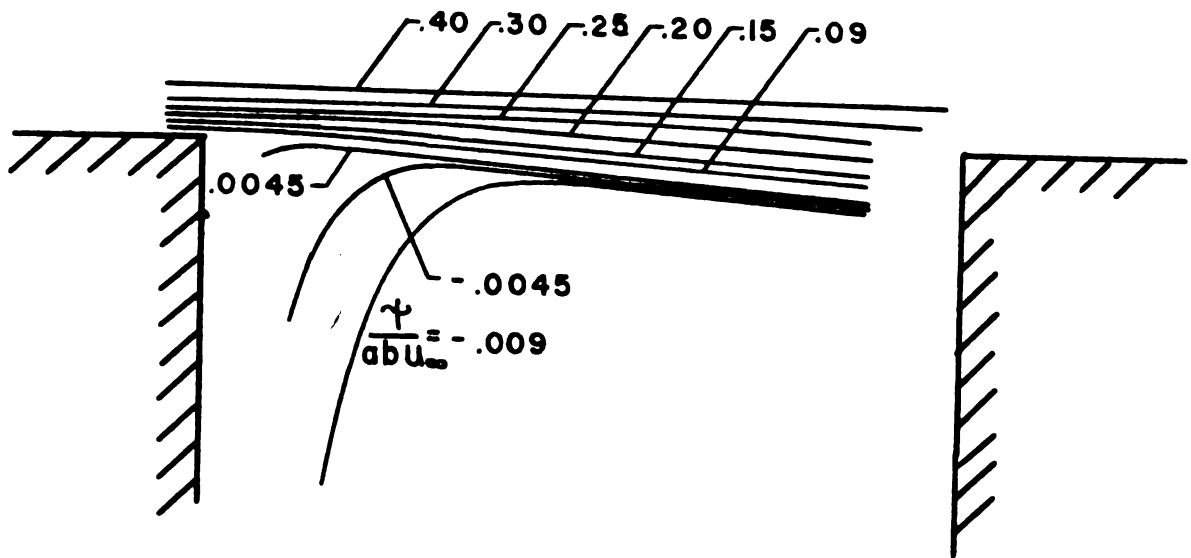


FIGURE 24
 PLOT OF CAVITY STREAMLINES
 CALCULATED FROM THE ANALYSIS
 ($h/b = 1.0$, $\delta/b = 0.1$)

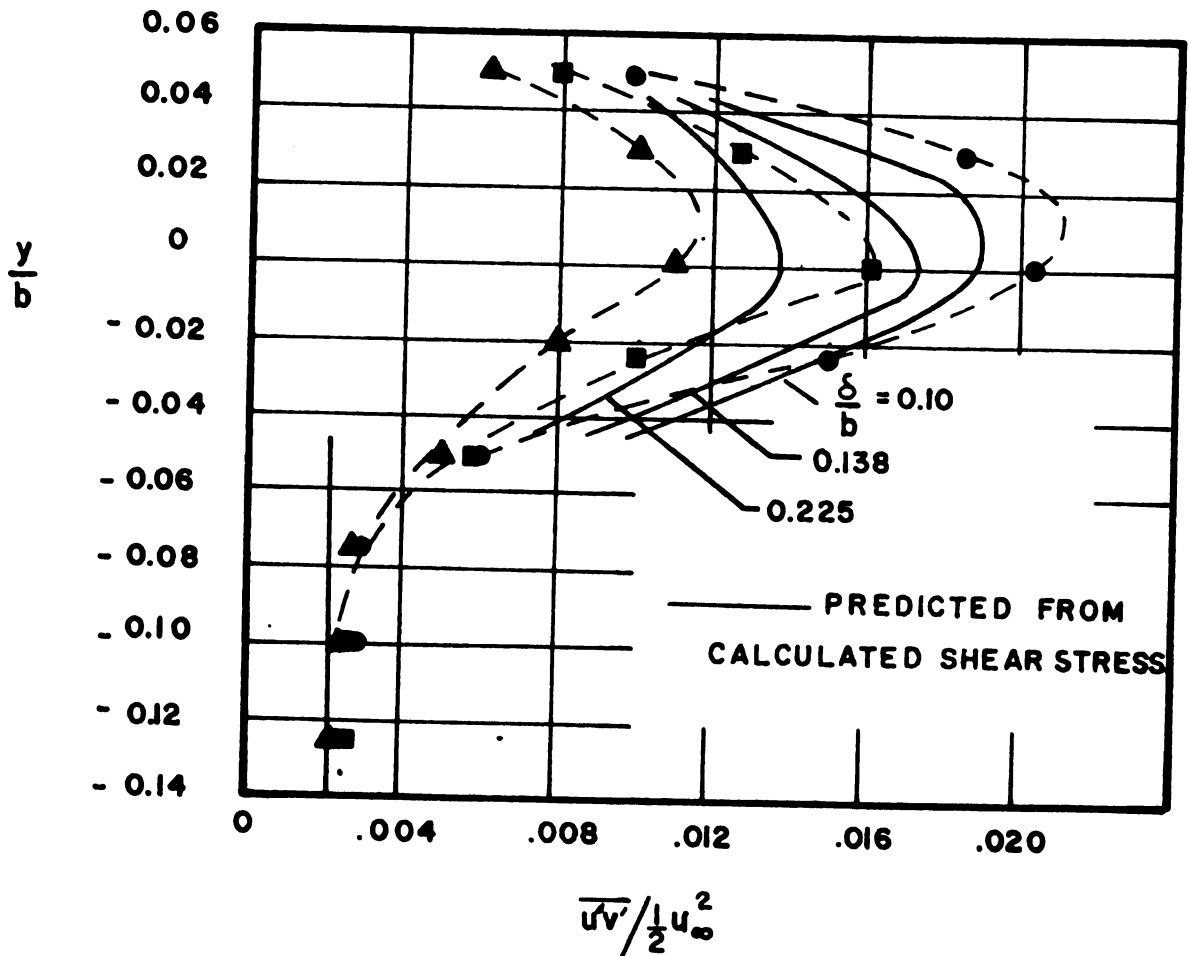
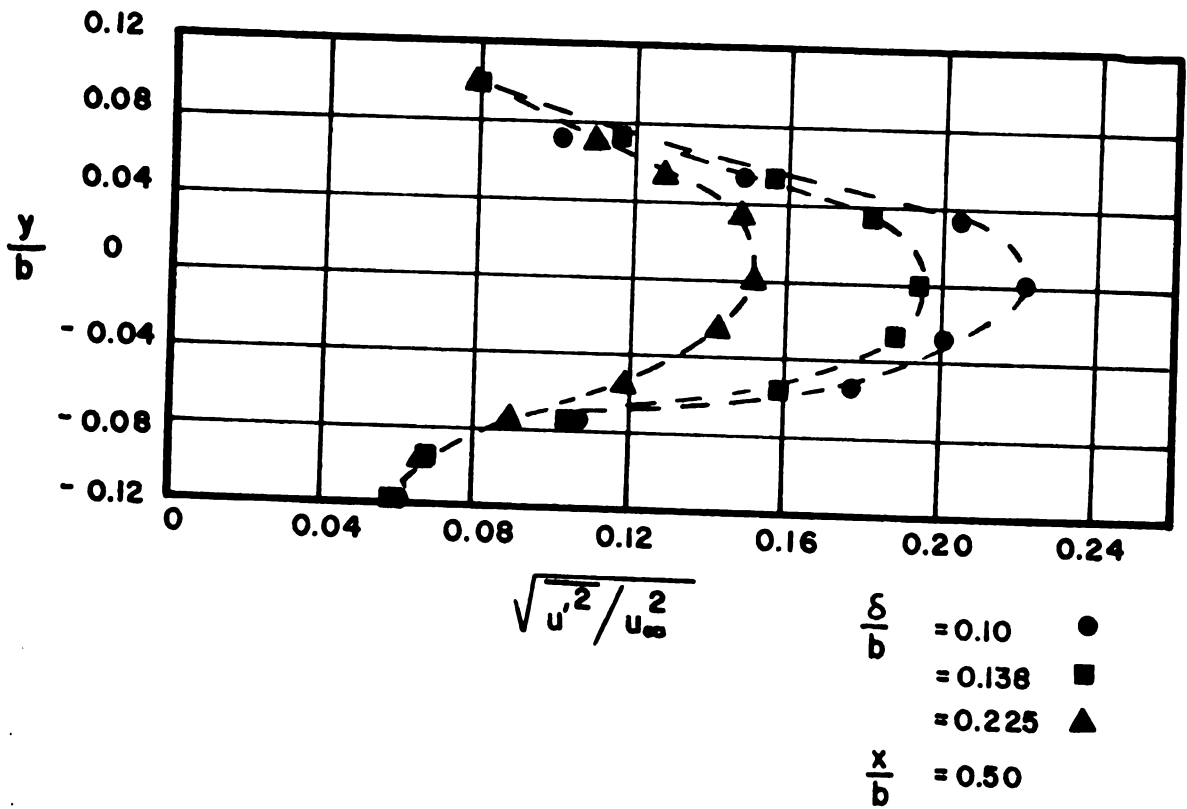


FIGURE 25
 TURBULENCE INTENSITY AND SHEAR
 DISTRIBUTIONS ($h/b = 1.0$)

fairly constant for y/b below -0.1 in the cavity. The cavity depth appears to have insignificant effects upon these four quantities when they are compared for similar values of δ/b .

4.5 Temperature

Temperatures that were measured at $x/b = 0.15, 0.50,$ and 0.85 from the frontside of the notch are shown in Figures 26 through 31. The temperatures are presented in the dimensionless ratio $(\bar{T} - T_{\infty}) / (T_w - T_{\infty})$. The temperatures T_w and T_{∞} were established as the average cavity wall temperature and the mid-channel free stream temperature respectively. A major temperature increase occurs across the shear layer. The temperature then remains nearly constant over the inviscid core with a second major temperature increase occurring near the surface. For deeper cavities, the influence of secondary eddies becomes noticeable. For the case of $h/b = 1.5$, the core temperature remains approximately uniform until reaching $y/b = -1.0$, at which time the temperature begins increasing. Because of the cavity size, this increase is hidden by the thermal boundary layer formed along the cavity floor. However, when the cavity depth is increased to $h/b = 2.0$, the sudden increase in temperature is easily seen. Again it is seen to occur at $y/b = -1.0$ indicating the formation of flow cells within the cavity. Burggraf, neglecting the influences of secondary eddies (with $Pr = 1$ and constant pressure)

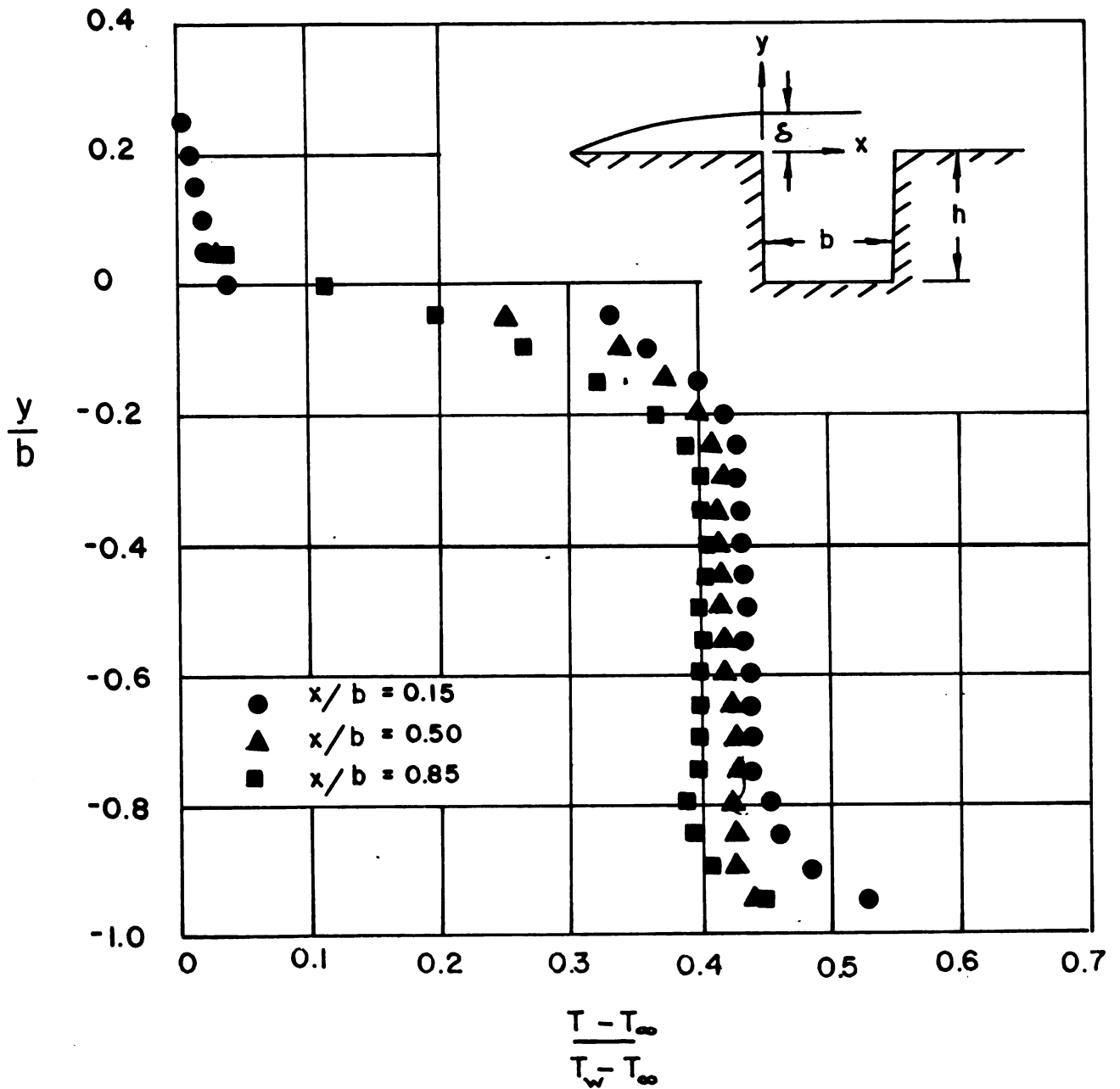


FIGURE 26
 TEMPERATURE PROFILES FOR
 $h/b = 1.0$ & $\delta/b = 0.28$

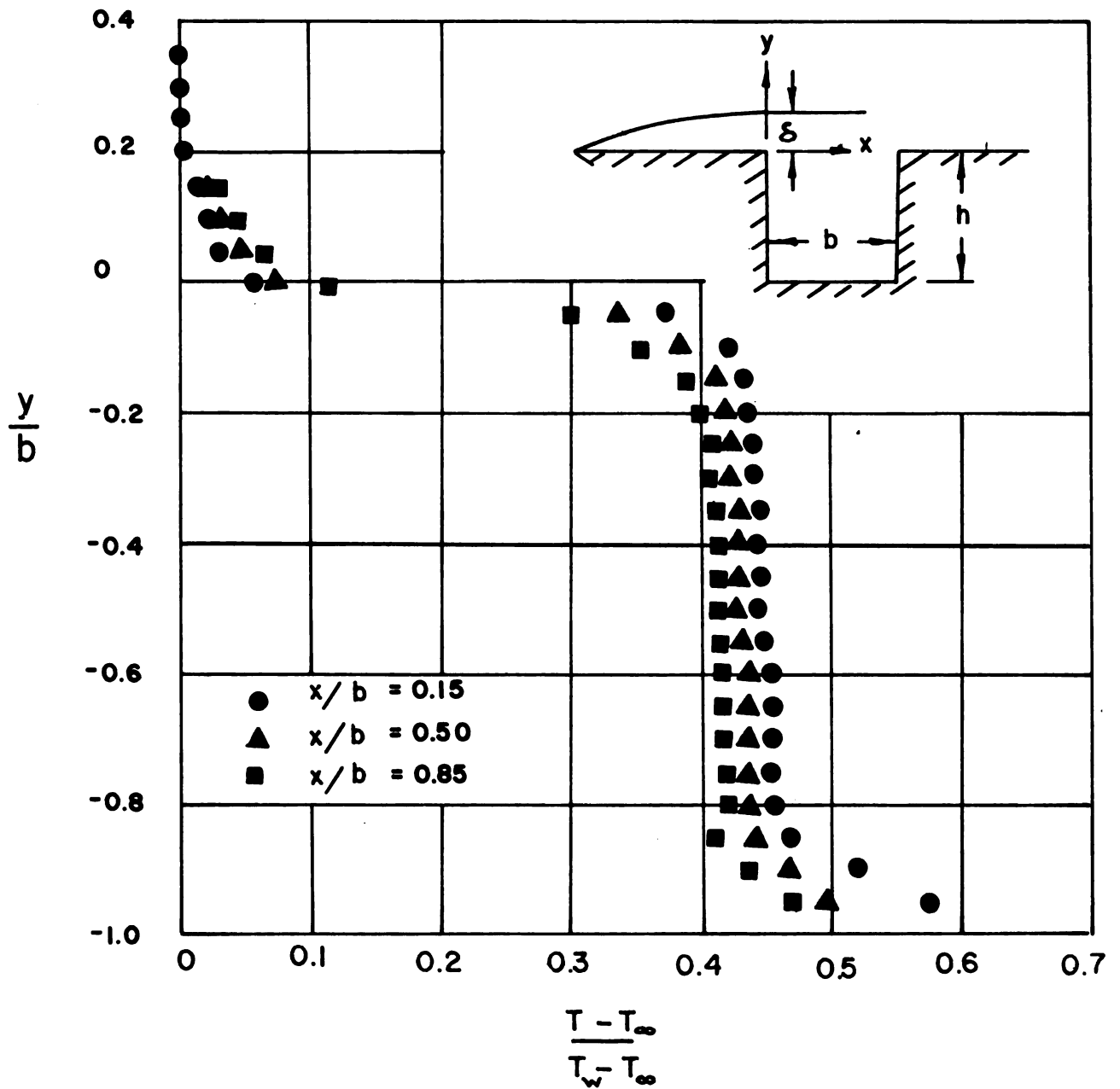


FIGURE 27
TEMPERATURE PROFILES FOR
 $h/b=1.0$ & $\delta/b=0.58$

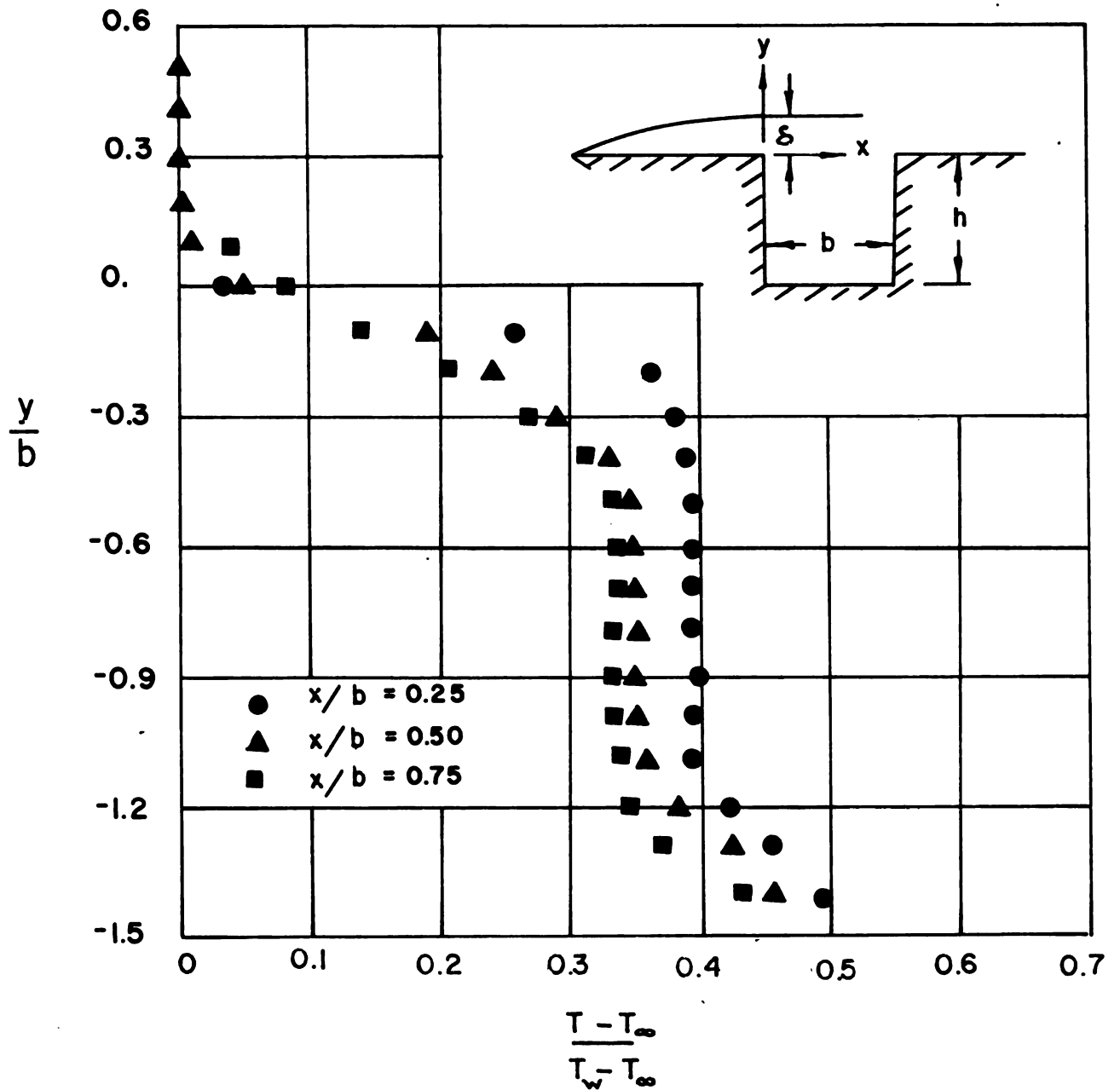


FIGURE 28
 TEMPERATURE PROFILES FOR
 $h/b=1.5$ & $\delta/b=0.56$

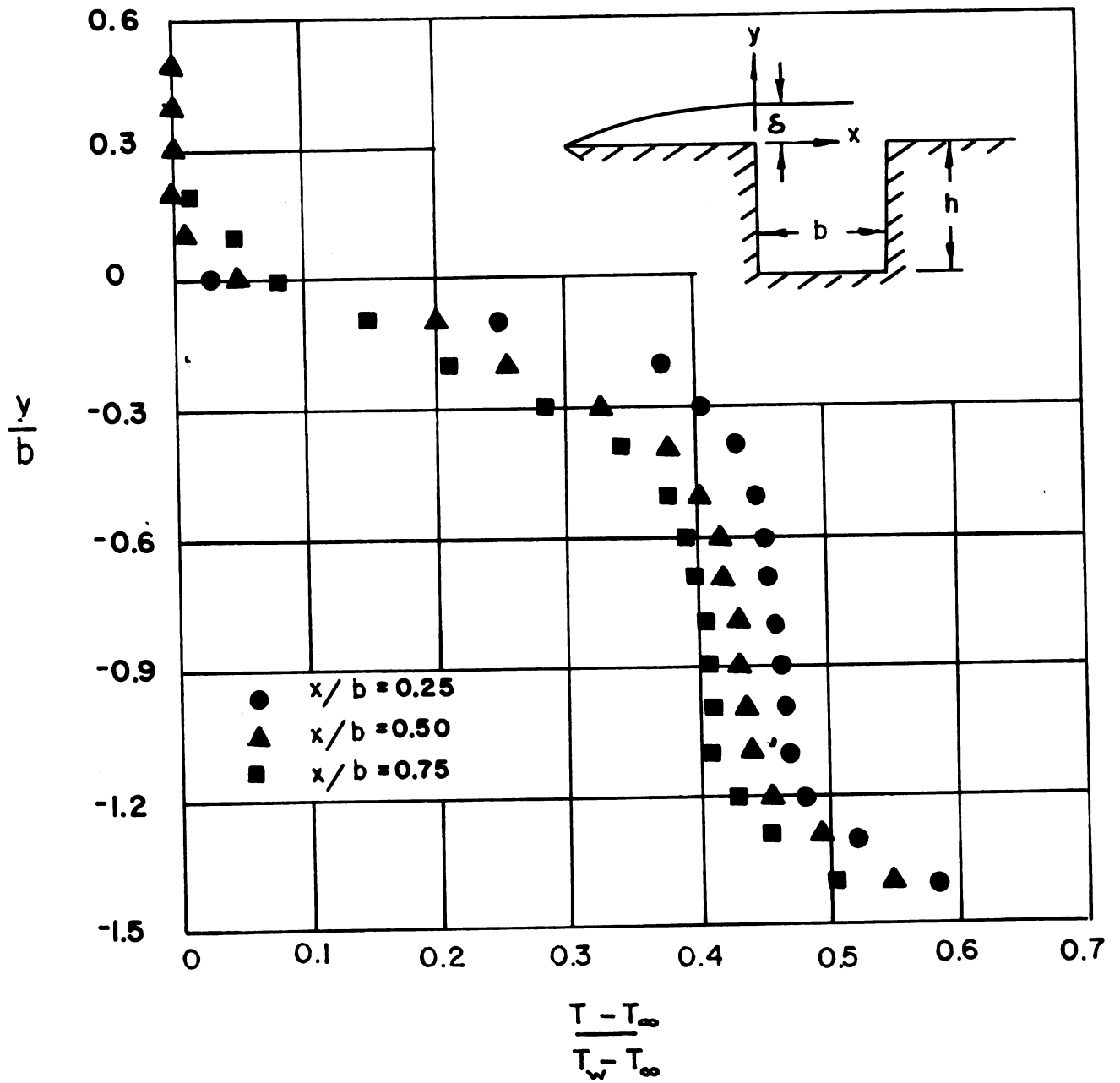


FIGURE 29
TEMPERATURE PROFILES FOR
 $h/b=1.5$ & $\delta/b=0.79$

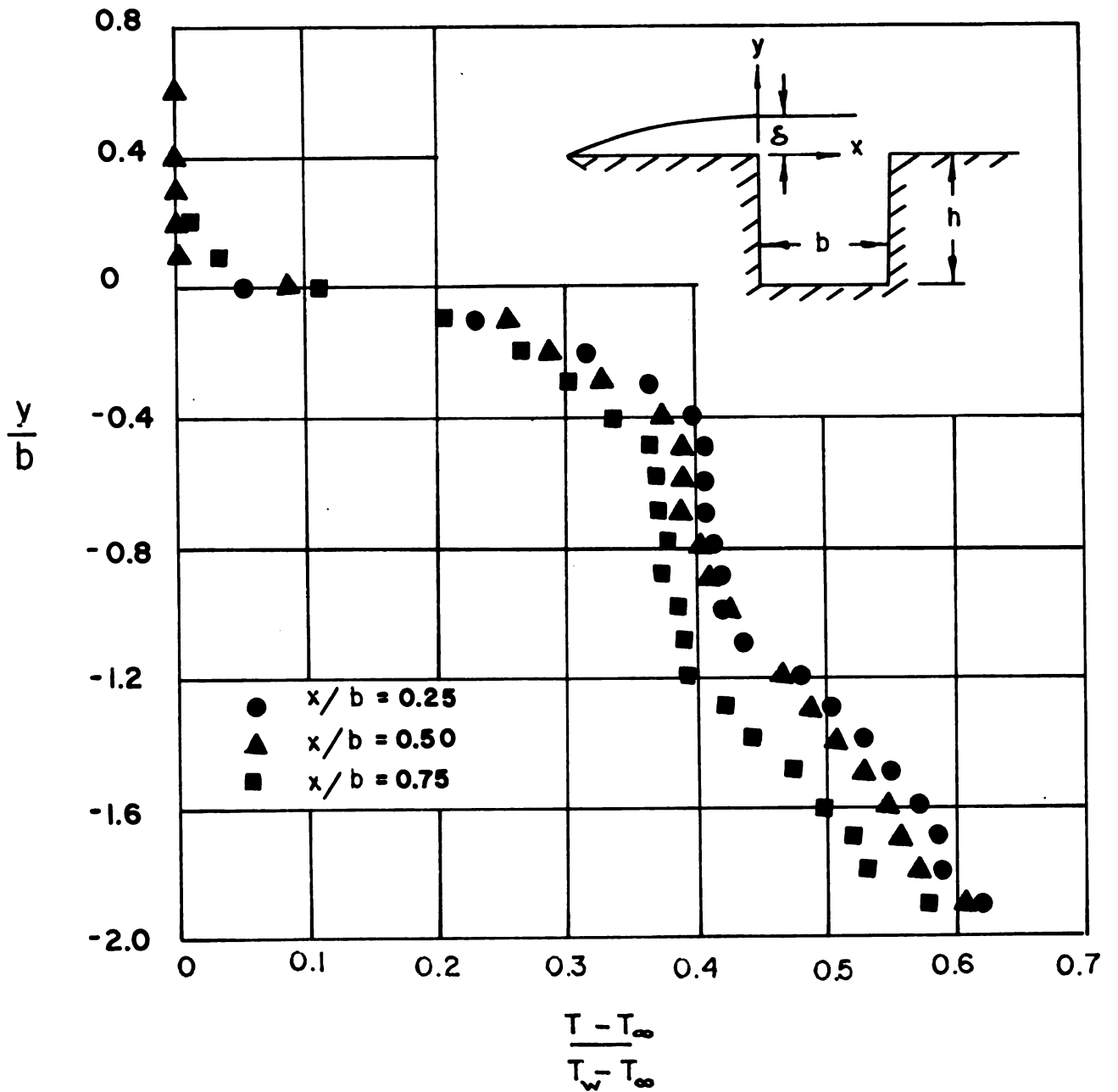


FIGURE 30
 TEMPERATURE PROFILES FOR
 $h/b = 2.0$ & $\delta/b = 0.38$

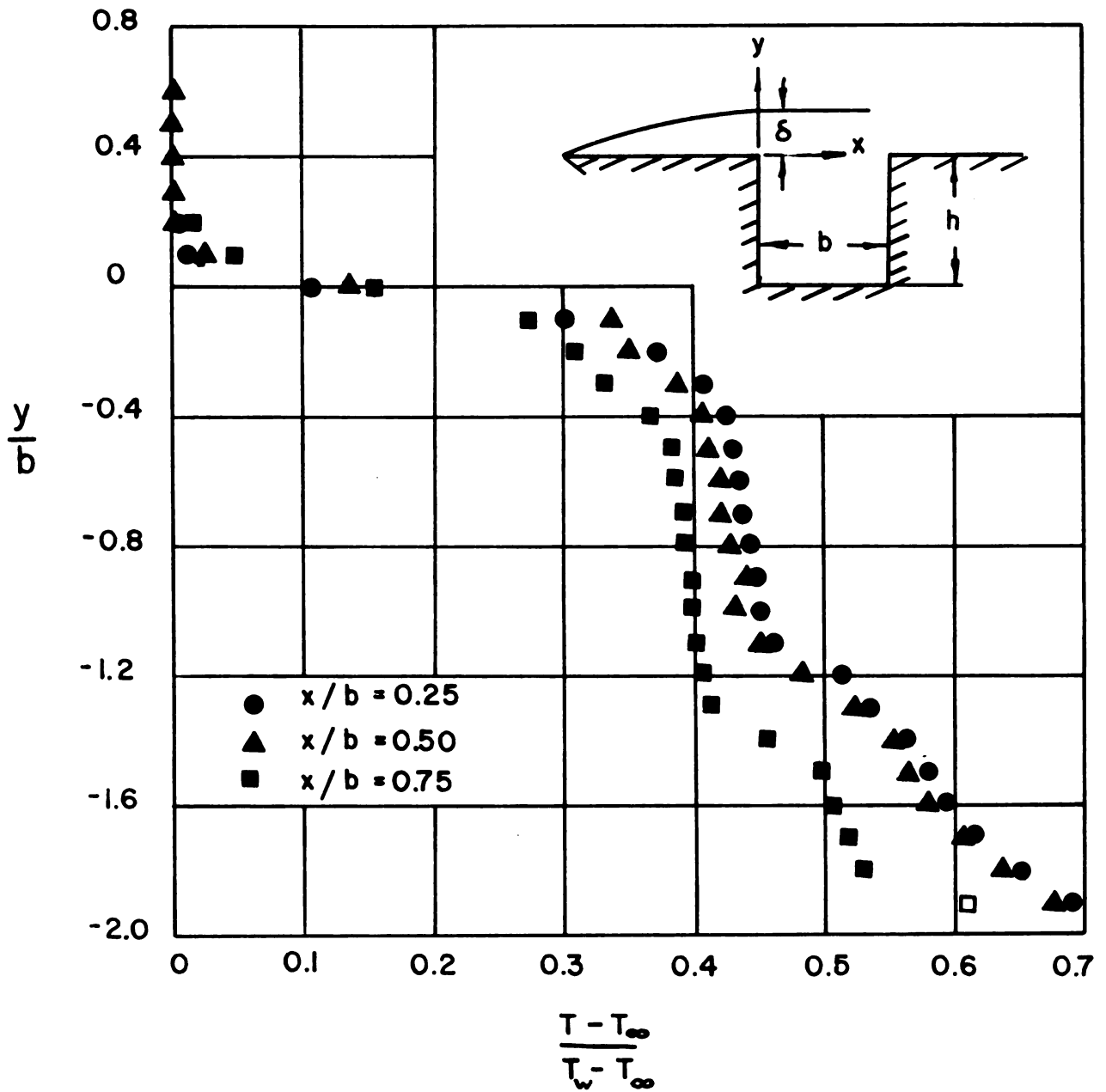


FIGURE 31
 TEMPERATURE PROFILES FOR
 $h/b = 2.0$ & $\delta/b = 0.76$

gives for the average inviscid core temperature T_o ,

$$\frac{T_o - T_\infty}{T_w - T_\infty} = \frac{1}{\sqrt{2(1 + b/h)}}$$

This value has been shown (analytically) to agree very well for laminar flow and $h/b = 1.0$ (12). For the present case (turbulent flow and variable h/b) a comparison between measured and predicted values is shown in Figure 32. Although the predicted values are consistently high, the correlation is adequate. However, as shown in Figure 32 a closer correlation is found using the equation:

$$\frac{T_o - T_\infty}{T_w - T_\infty} = \frac{1}{\sqrt{3(1 + b/h)}}$$

Using this expression for T_o , equations (3.38) and (3.50) were solved. The resulting expressions for $\theta(\eta)$ are shown in Figures 33 through 36 where they are seen to correlate closely with the experimental data.

4.6 Heat Transfer

The results from the measurements of the average heat transfer from a heated cavity are shown in Figure 38. The form of the heat-transfer coefficient was taken as

$$\overline{St} = \frac{\overline{q}}{\rho C_p u_\infty (T_o - T_\infty)}$$

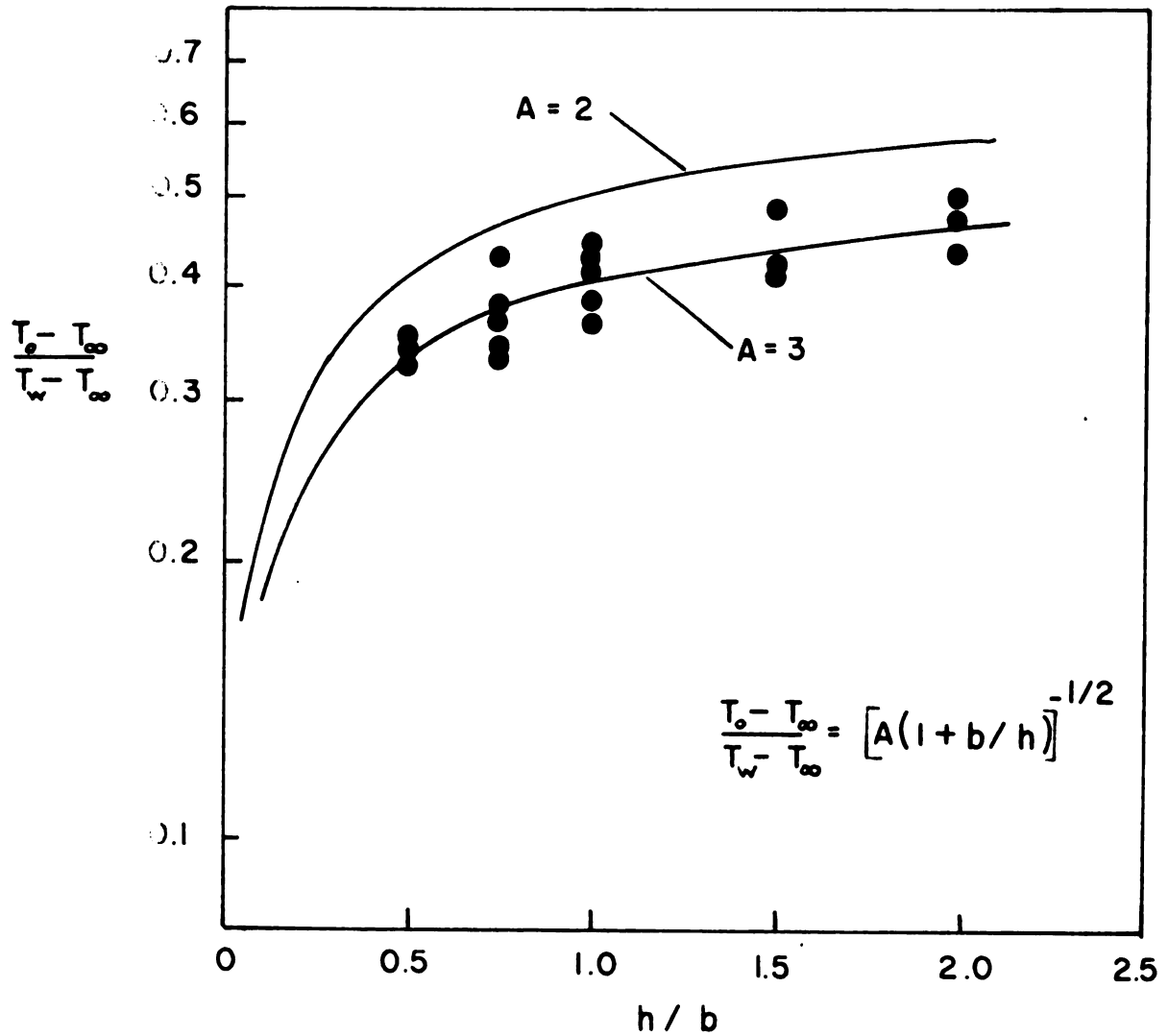


FIGURE 32
 PREDICTED CAVITY BULK TEMPERATURE
 AND COMPARISON WITH EXPERIMENTAL DATA

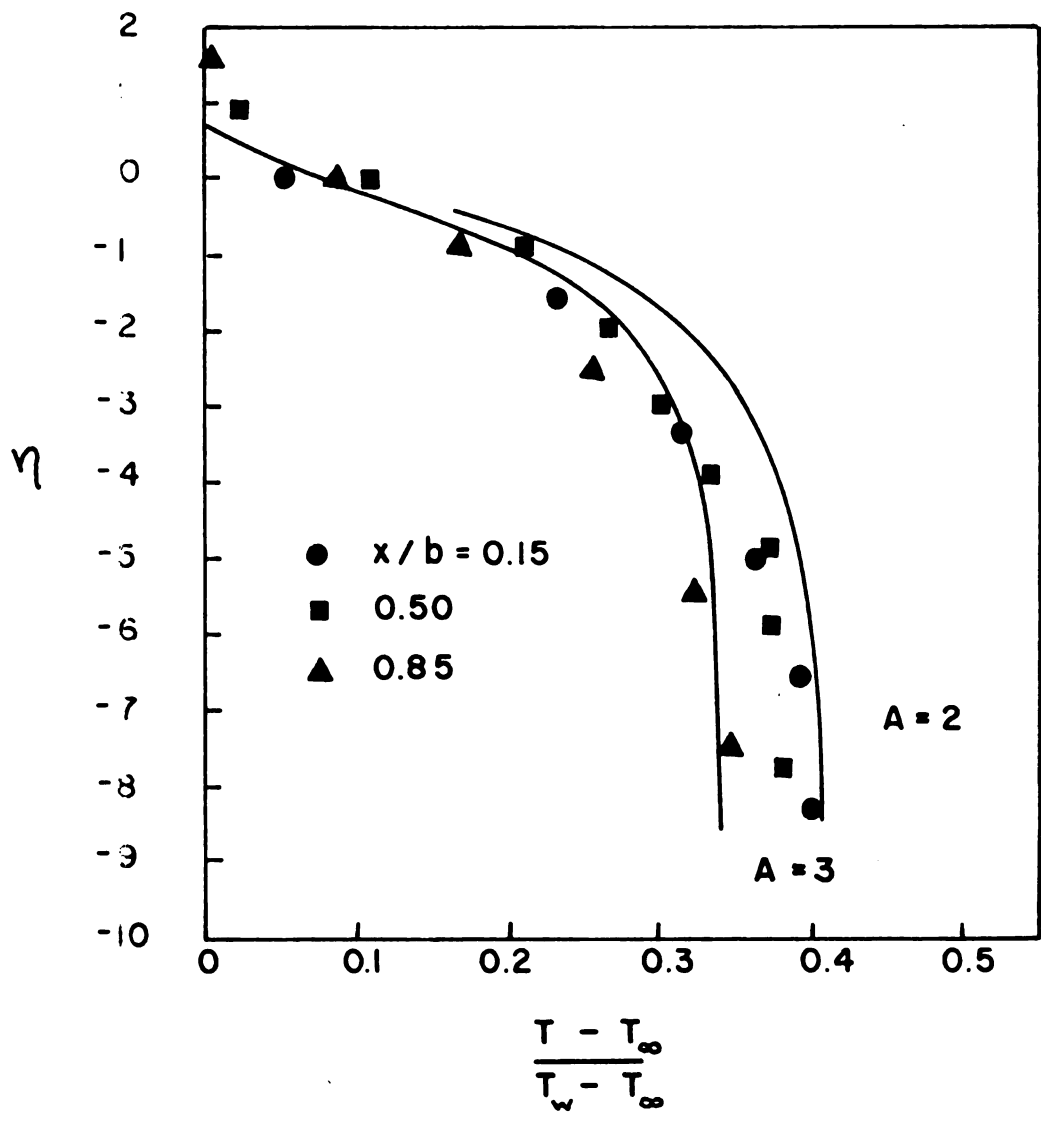


FIGURE 33
 PREDICTED AND MEASURED TEMPERATURE
 PROFILES ($h/b = 0.50$, $\delta/b = 0.21$)

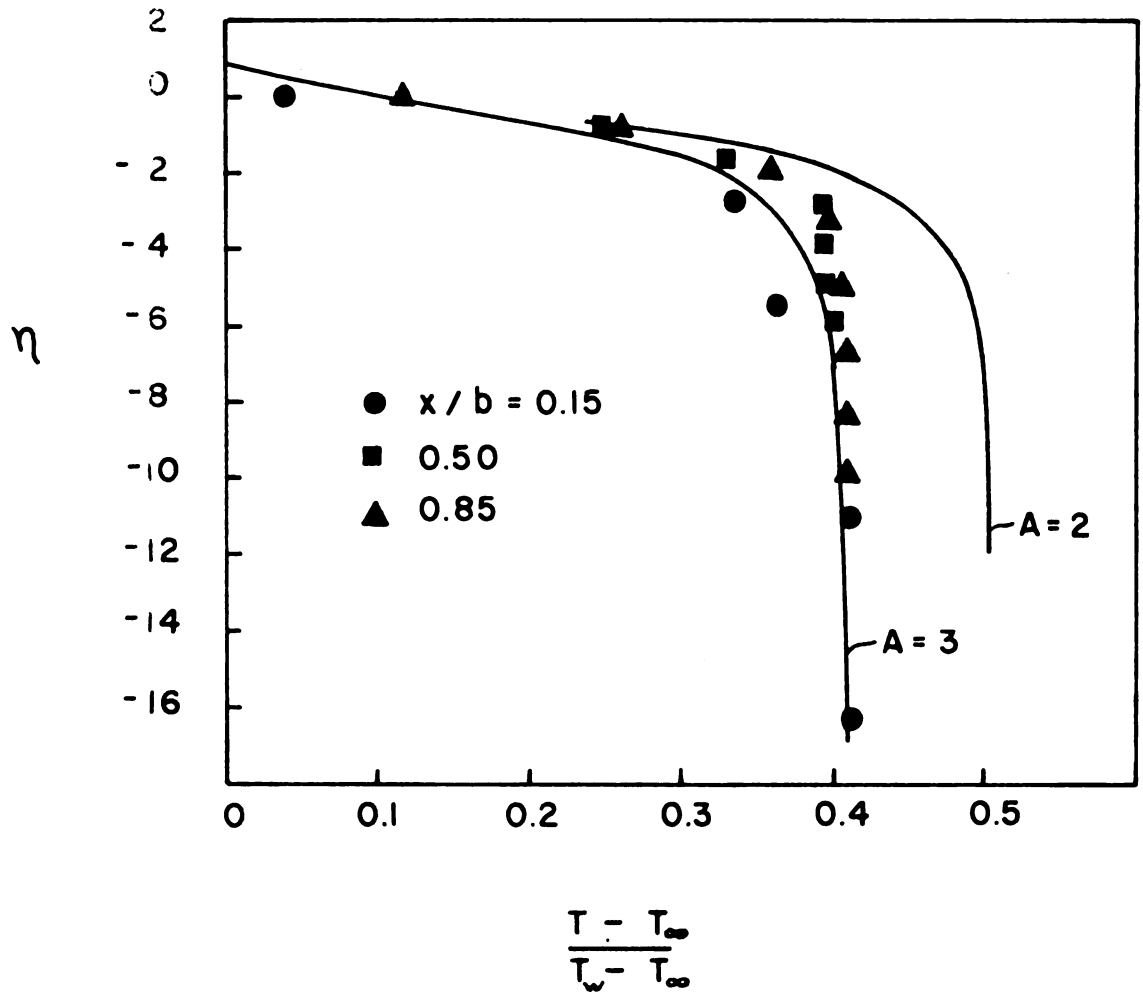


FIGURE 34
 PREDICTED AND MEASURED TEMPERATURE
 PROFILES ($h/b=1.0$, $\delta/b=0.28$)

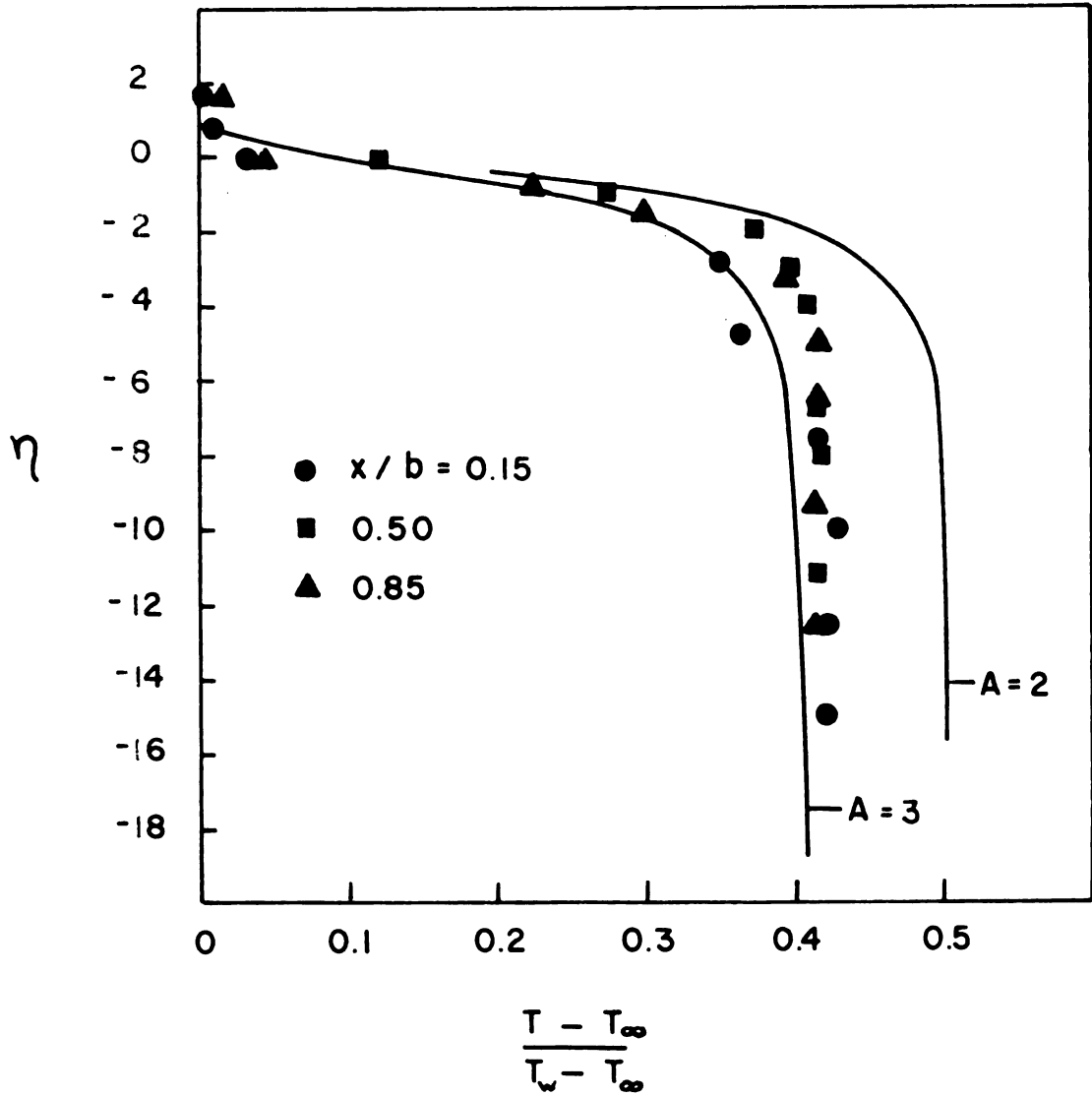


FIGURE 35

PREDICTED AND MEASURED TEMPERATURE
 PROFILES ($h/b = 1.0$, $\delta/b = 0.58$)

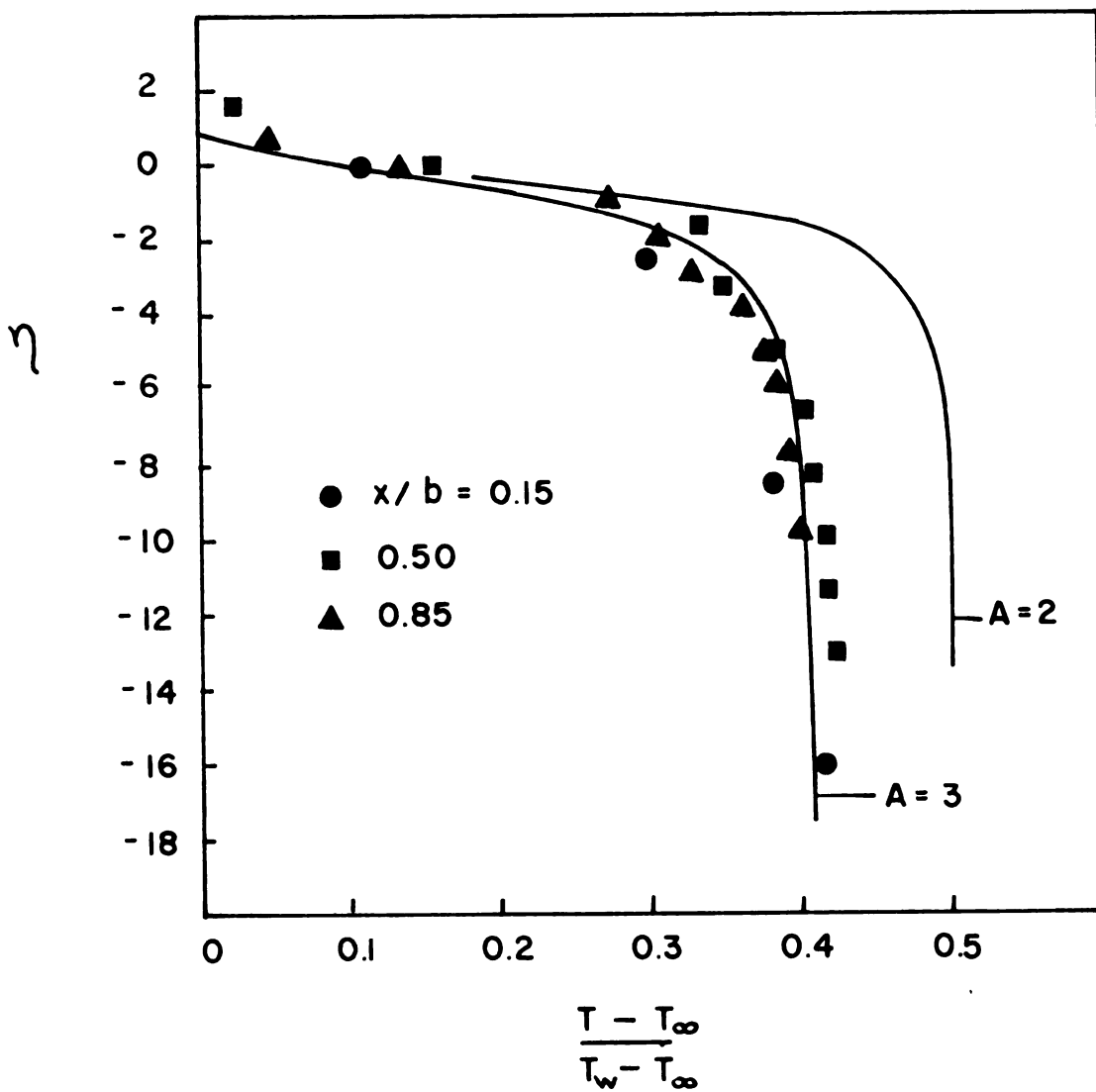


FIGURE 36
PREDICTED AND MEASURED TEMPERATURE
PROFILES ($h/b = 1.0, \delta/b = 0.76$)

To correlate the data, reference is made to equation (3.55) where the semi-theoretical expression describing the heat transfer is derived. Since the Stanton number is defined in terms of the temperature difference $(T_o - T_\infty)$ rather than $(T_w - T_\infty)$, the results are independent of cavity depth. This result is confirmed reasonably well by the experimental data (Figure 38).

Additional heat transfer data is presented in Figures 37 and 39. Here local heat transfer rates measured along the cavity walls are given with the heat transfer coefficient taken as:

$$St = \frac{q}{\rho C_p u_\infty (T_w - T_\infty)}$$

q is the heat liberated per unit time and per unit exposed surface area of the ribbon heating elements. The heat rate was deduced from the measured power which was used to heat the series-connected ribbons. The heat transfer rates are greatest at the top of the downstream side, most probably due to the impinging external flow. The heat transfer rates decrease rapidly through this zone remaining somewhat uniform along the remainder of the downstream wall. Secondary peaks appear along the bottom and upstream walls, with these rates then decreasing slightly along the direction of flow. The relative size of the oncoming boundary layer also influences the local heat transfer rates and is most pronounced in the impingement region of the downstream wall.

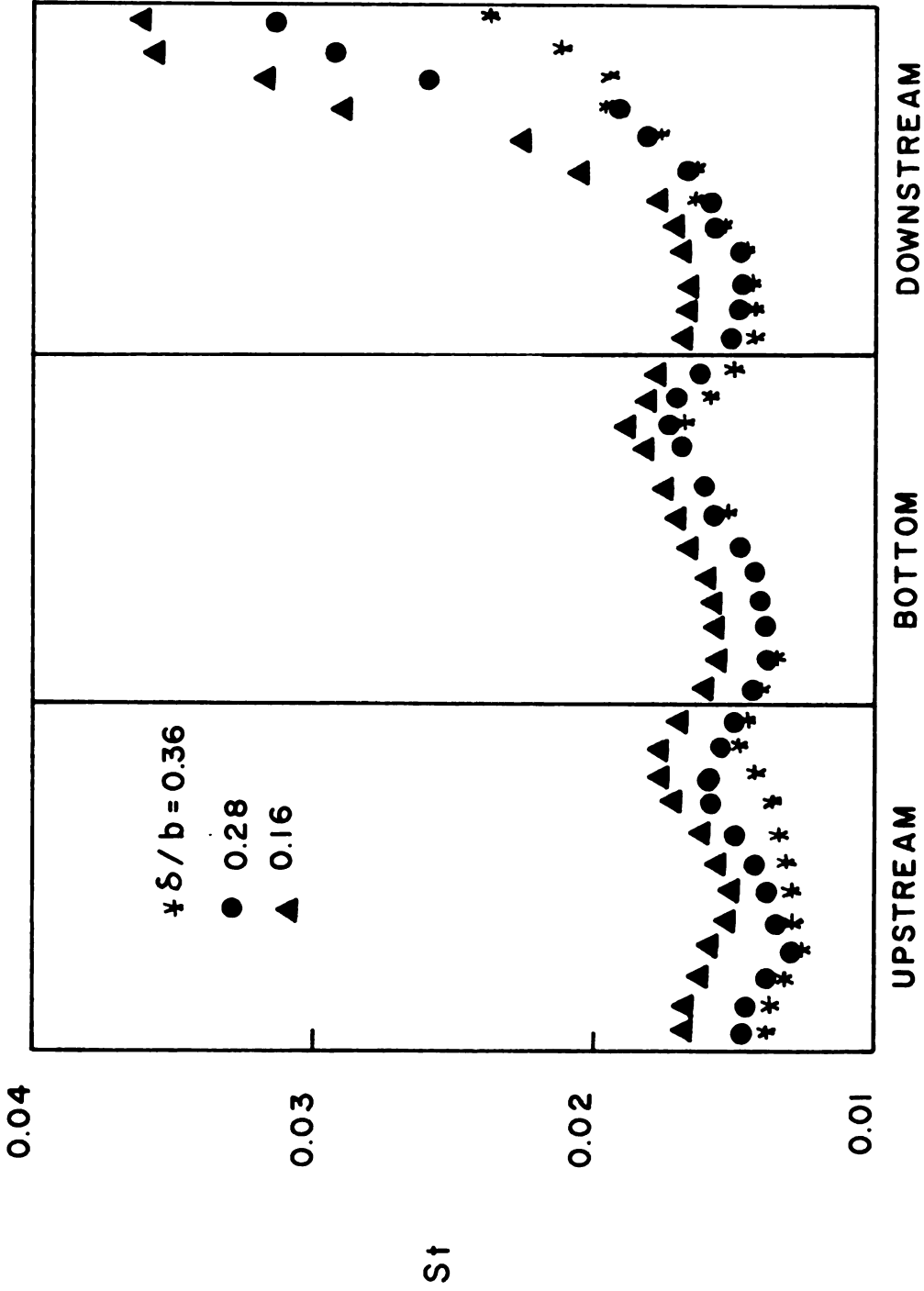


FIGURE 37
 LOCAL CAVITY HEAT TRANSFER RATES
 ($h/b = 1.0$)

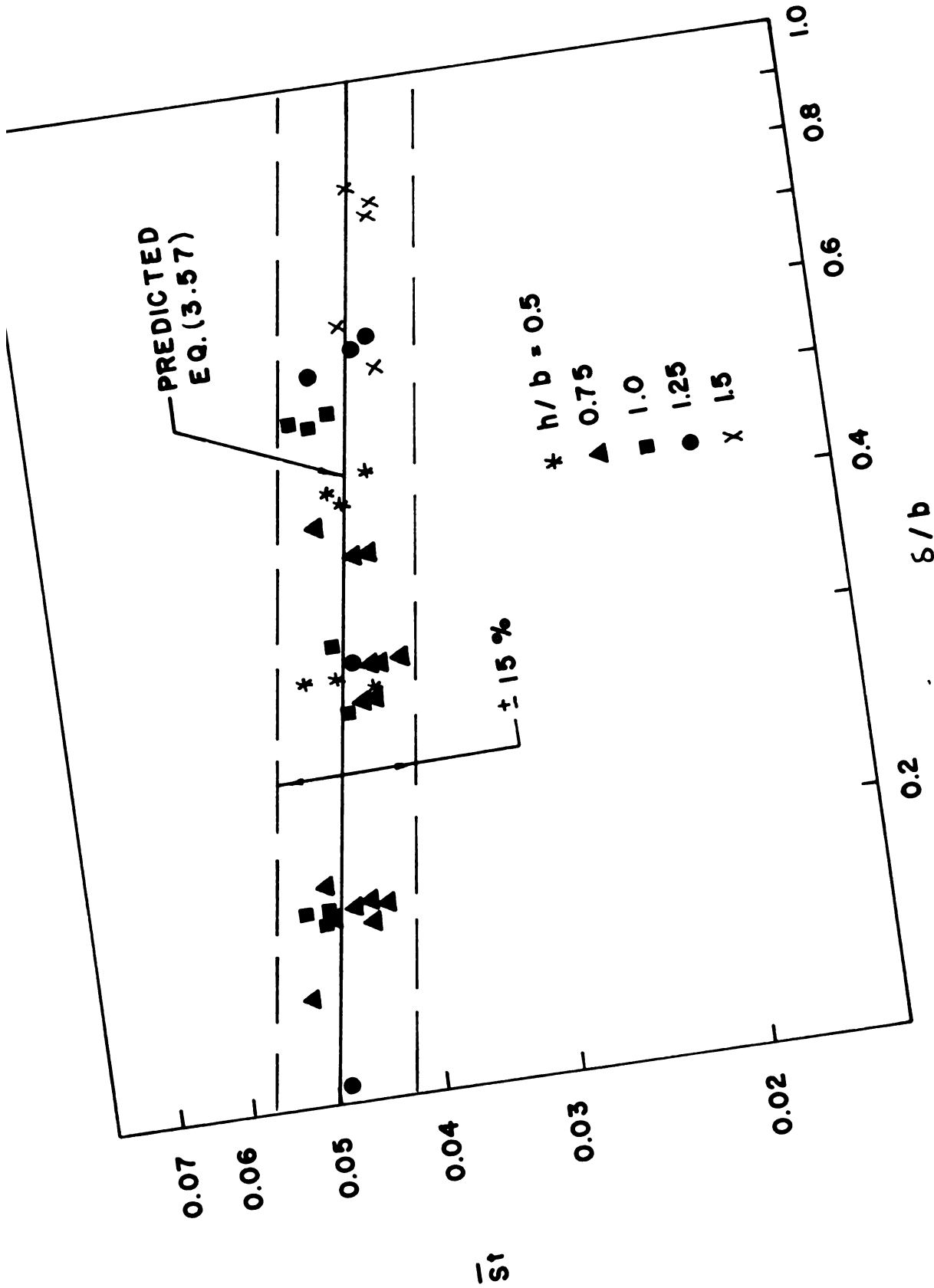


FIGURE 38
AVERAGE HEAT TRANSFER FROM A HEATED CAVITY
(BASED ON AVERAGE HEAT TRANSFER RATES)

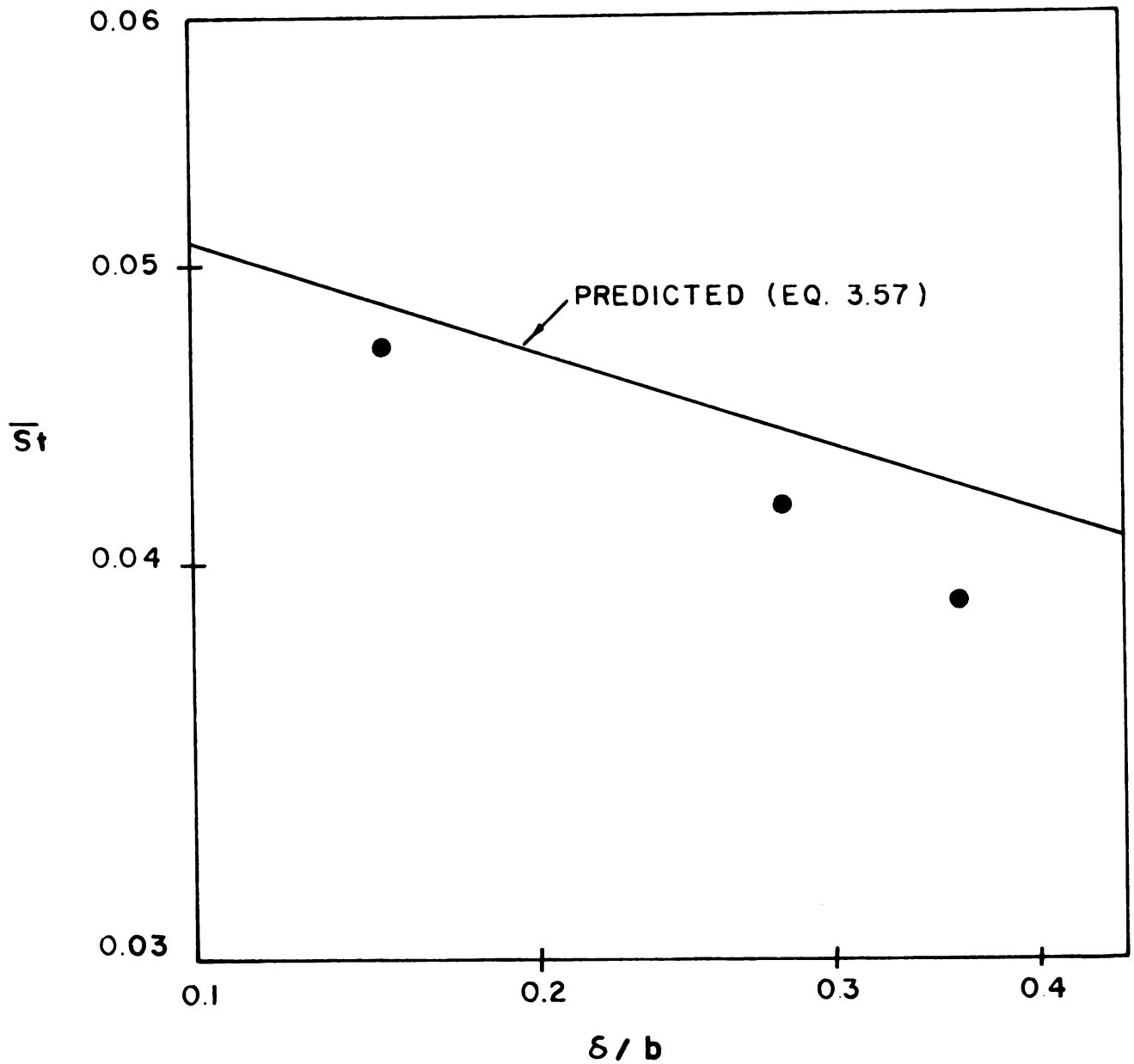


FIGURE 39
AVERAGE HEAT TRANSFER FROM A HEATED CAVITY
(DATA BASED ON LOCAL HEAT TRANSFER RATES)
($h/b = 1.0$)

5. CONCLUSIONS

1. The expression for the predicted velocity distribution as given by equation (3.20) correlates the data reasonably well with a maximum deviation of 20 percent within a substantial portion of the flow. The coefficient "a" was taken as 0.12. For a plane free jet, a value for "a" of 0.09 has been established (14). Evidently, this increase in "a" is due to the additional shear layer turbulence caused by the cellular flow within the cavity.

2. The experimental distribution of percent turbulence and turbulent shear stress (Figure 24) have maximum values at a point coinciding with the dividing streamline ($y = 0$) and are both quite sensitive to changes in the relative size of the approaching boundary layer.

The predicted distribution for the turbulent shear distribution (Figure 24) is compared with the hot wire measurements well within ± 20 percent.

3. The time-averaged temperature distribution described by equations (3.38) and (3.50) correlates the data reasonably well with the coefficient C taken as 1.4 giving the best correlation with experiment. The average inviscid core temperature T_o is seen to be

adequately determined by Burggraf's equation:

$$\frac{T_o - T_\infty}{T_w - T_\infty} = \frac{1}{\sqrt{A (1 + b/h)}}$$

However, the present study indicates that for turbulent flow a value of 3.0 for the constant A gives better agreement with experiment.

With this temperature difference ($T_o - T_\infty$) used in this definition, the average Stanton number is seen to be independent of the relative cavity depth. The average heat transfer in the cavity (Equation 3.56) was confirmed within ± 15 percent by experiment and is closely approximated by the correlation:

$$\overline{St} = 0.0365 \left(\frac{\delta}{b} \right)^{-0.1367}$$

REFERENCES

1. Fox, Jay, "Surface Pressure and Turbulent Airflow in Transverse Rectangular Notches," NASA Technical Note D-2501, 1964.
2. Charwat, A. F., et al, "An Investigation of Separated Flows -- Part I: The Pressure Field," Journal of the Aero/Space Sciences, Vol. 28, p. 457, 1961.
3. Charwat, A. F., et al, "An Investigation of Separated Flows -- Part II: Flow in the Cavity and Heat Transfer," Journal of the Aero/Space Sciences, Vol. 28, pp. 513-527, 1961.
4. Larson, H. K., "Heat Transfer in Separated Flows," Journal of the Aero/Space Sciences, Vol. 26, No. 11, pp. 731-38, November, 1959.
5. Wieghardt, K., "Erhöhung des turbulenten Reibungswiderstandes durch Oberflächenstörungen." Forschungshefte für Schiffstechnik, Heft 2, pp. 65-81, 1953.
6. Tillmann, W., "Neue Widerstandsmessungen an Oberflächenstörungen in der turbulenten Reibungsschicht. Forschungshefte für Schiffstechnik, Heft 2, pp. 81-88, 1953.
7. Roshko, A., "Some Measurements of Flow in a Rectangular Cutout." NACA Tech. Note No. 3488, 1955.
8. Tani, I., Tuchi, M., and Komodo, H., "Experimental Investigation of Flow Separation Associated with a Step or a Groove," Aeronautical Research Institute, University of Tokyo, Report No. 364, April, 1961.
9. Seban, R. A., Emery, A., and Levy, A., "Heat Transfer to Separated and Reattached Subsonic Turbulent Flows Obtained Downstream of a Surface Step," Journal of the Aero/Space Sciences, Vol. 26, No. 12, pp. 809-814, December, 1959.

10. Seban, R. A. and Fox, J., "Heat Transfer to the Air Flow in a Surface Cavity," Proceedings of the 1961 International Heat Transfer Conference, ASME, p. 426.
11. Chapman, D. R., "A Theoretical Analysis of Heat Transfer in Regions of Separated Flow," NACA TN 3792, 1966.
12. Burggraf, Odus R., "A Model of Steady Separated Flow in Rectangular Cavities at High Reynolds Number," Proceedings of the 1965 Heat Transfer and Fluid Mechanics Institute, The Standord University Press, p. 190.
13. Hinze, J. O., Turbulence, McGraw-Hill Book Company, Inc., New York, p. 104, 1959.
14. Abramovich, G. N., The Theory of Turbulent Jets, The M.I.T. Press, Cambridge (Mass.), 1963, pp. 61-63.
15. Batchelor, G, K., "On Steady Laminar Flow with Closed Streamlines at Large Reynolds Numbers," Journal of Fluid Mechanics, Vol. 1, p. 177, 1956.
16. Flow Corporation "Model HWB2 Hot Wire Anemometer Theory and Instruction," Flow Corp. Bulletin No. 37B, 1958.
17. Boussinesq, J., "Essai sur la theorie des eaux courantes," Memoires presentes par divers savants a l'Academie des Sciences 23, 1877.

APPENDIX

Table 1.--Velocity data, $h/b = 1.0$.

\bar{u} , x-component of time mean velocity (ft./sec.)									
y/b	x/b = 0.15			x/b = 0.50			x/b = 0.85		
	δ/b	.10	.30	.50	.10	.30	.50	.10	.30
0.60			99.5			100.1			105.0
0.55			99.5			100.3			104.8
0.50			99.5			100.0			104.8
0.45			97.0			100.0			104.8
0.40		99.2	95.0		100.0	96.9		105.0	102.0
0.35		99.3			100.0			104.8	97.6
0.30		99.3	92.0		100.0	94.0		105.0	97.5
0.25					95.8			102.5	94.0
0.20	100.0	93.0	87.5	100.3	95.8	89.4	105.0	98.2	92.2
0.15	100.0			100.0	90.5		104.8	94.8	86.3
0.10	100.0	87.0	81.5	100.3	86.0	77.3	105.1	89.4	83.0
0.05	88.5	78.0	70.0	91.5	75.7		94.5	80.2	73.5
0	64.0	63.5	55.5	56.1	60.5	56.1	71.2	64.6	63.0
-0.05	25.5	29.5	18.0	33.6	27.2	28.4	41.5	41.6	42.3
-0.10	25.0	22.5	13.5	29.4	21.2	20.7	31.3	31.5	31.4
-0.15	22.5	20.0		26.5	20.3		24.4	23.0	23.3
-0.20	21.0	16.0	12.5	22.8	18.7	14.2	24.6	19.6	21.1
-0.25		10.0		15.4	13.3		21.3	17.5	24.5
-0.30	19.5	10.0	11.5	12.4	11.2	8.1	20.4	16.7	22.4
-0.40	17.5	10.0	11.0	11.4	4.8	4.6	15.7	14.7	19.9
-0.50	16.0	5.0	10.0	8.1	4.1	4.1	13.3	14.7	19.1

Table 2.--Velocity data, $h/b = 2.0$.

\bar{u} , x-component of time mean velocity (ft./sec.)										
y/b	$x/b = 0.15$			$x/b = 0.50$			$x/b = 0.85$			
	δ/b	.10	.30	.50	.10	.30	.50	.10	.30	.50
0.60				100.0						100.5
0.55				99.5			100.3			100.5
0.50				99.7			100.3			100.5
0.45										101.9
0.40		100.0	95.5		100.3	97.7		104.8	100.0	
0.35		99.7			100.3			105.0	96.9	
0.30		100.0	92.0		100.3	91.9		105.0	95.3	
0.25					97.9			102.5	93.7	
0.20	100.0	92.5	88.0	99.7	94.4	86.9		98.7	89.6	
0.15	100.0			100.1	92.6			105.0	94.7	86.4
0.10	100.0	83.5	78.5	100.3	85.0	76.5	104.7	88.0	81.5	
0.05	87.0	76.5	69.5	90.4	77.8		96.3	80.4	69.6	
0	50.0	56.5	50.0	60.1	57.6	51.9	74.2	61.6	59.6	
-0.05	20.1	19.5	22.0	30.0	22.8	23.7	42.0	36.2	36.7	
-0.10	19.5	16.5	15.0	25.5	22.2	19.1	38.2	25.9	26.4	
-0.15	15.1	14.2		20.4	19.2		31.8	20.4	25.2	
-0.20	13.5	12.5	8.0	15.3	18.4	17.9	27.7	17.0	22.4	
-0.25		12.5			11.6		22.7	15.1	20.4	
-0.30	12.5	12.5	6.0	10.5	10.6	10.1	22.7	13.9	20.4	
-0.40	11.5	8.5	5.0	7.5	9.7	7.2	17.3	12.9	18.9	
-0.50	10.5	9.9	5.0	5.5	8.7	5.5	14.1	12.3	16.5	

Table 3.--Turbulence data.

$\frac{y}{b}$	$\frac{\delta}{b}$	$(h/b = 1.0)$			$(h/b = 2.0)$		
		$\frac{-\overline{u'v'}}{\frac{1}{2}u_\infty^2}$	$\frac{-\overline{u'v'}}{\bar{u}^2}$	$\frac{\sqrt{\overline{u'^2}}}{\sqrt{u_\infty^2}}$	$\frac{-\overline{u'v'}}{\frac{1}{2}u_\infty^2}$	$\frac{-\overline{u'v'}}{\bar{u}^2}$	$\frac{\sqrt{\overline{u'^2}}}{\sqrt{u_\infty^2}}$
0.10	0.10			.060			.061
0.075		.005	.0109	.084	.004	.010	.080
0.050		.010	.0244	.148	.010	.024	.150
0.025		.019	.0579	.205	.018	.059	.215
0		.021	.108	.223	.023	.115	.225
-.025		.015	.174	.200	.017	.185	.215
-.050		.006	.169	.178	.007	.173	.180
-.075		.003	.090	.114	.004	.090	.124
-.100		.003	.099	.077	.003	.110	.115
-.125		.0025	.090	.057	.0025	.090	.075
-.150		.003	.107		.002	.110	.070
-.175		.0025	.102		.0025	.100	
0.10	0.138			.060			.060
0.075		.005	.0117	.098	.005	.012	.110
0.050		.008	.0275	.138	.009	.029	.143
0.025		.0125	.0412	.182	.013	.041	.182
0		.016	.0885	.198	.017	.091	.203
-.025		.010	.124	.190	.011	.125	.193
-.050		.006	.173	.161	.007	.184	.172
-.075		.003	.096	.114	.005	.097	.115
-.100		.0025	.089	.077	.003	.092	.082
-.125		.0025	.092	.057	.002	.092	.057
-.150		.0025	.099		.002		
0.075	0.225	.005	.0124	.089	.005	.0125	.090
0.05		.006	.0192	.127	.005	.019	.126
0.025		.010	.0355	.148	.010	.040	.152
0		.011	.066	.152	.012	.069	.155
-.025		.008	.109	.141	.009	.110	.141
-.050		.005	.170	.100	.005	.170	.110
-.075		.003	.106	.077	.003	.106	.074
-.100		.0025	.096	.057	.003	.090	.050
-.125		.0025	.105	.057	.002	.110	.050
-.150		.0020	.0925				

Table 4.--Temperature data ($x/b = 0.5$).

		$\left(\frac{h}{b} = 1.0\right)$ $\left(\frac{\delta}{b} = 0.28\right)$		$\left(\frac{h}{b} = 1.0\right)$ $\left(\frac{\delta}{b} = 0.58\right)$		$\left(\frac{h}{b} = 2.0\right)$ $\left(\frac{\delta}{b} = 0.38\right)$		$\left(\frac{h}{b} = 2.0\right)$ $\left(\frac{\delta}{b} = 0.76\right)$	
$\frac{y}{b}$	T °F	$\frac{T-T_\infty}{T_w-T_\infty}$	T	$\frac{T-T_\infty}{T_w-T_\infty}$	$\frac{y}{b}$	T	$\frac{T-T_\infty}{T_w-T_\infty}$	T	$\frac{T-T_\infty}{T_w-T_\infty}$
.25	80.0	.0044	76.0	0.0	.3	76.0	0.0	75.0	0.0
.20	80.0	.0044	76.0	0.0	.2	76.0	0.0	75.0	0.0
.15	80.1	.0055	78.0	.020	.1	78.2	.0022	77.4	0.24
.10	80.1	.0055	79.2	.032	0	84.6	.086	88.6	.136
.05	82.1	.0277	80.6	.046	-.1	98.9	.229	108.7	.337
0	83.1	.0388	83.2	.072	-.2	107.6	.316	110.0	.350
-.05	102.3	.251	109.6	.336	-.3	108.6	.326	113.7	.387
-.10	110.4	.341	114.3	.383	-.4	109.6	.376	115.6	.406
-.15	113.4	.374	117.0	.410	-.5	115.0	.390	116.0	.410
-.20	115.7	.400	117.7	.417	-.6	115.1	.391	117.0	.420
-.25	116.7	.411	118.5	.425	-.8	116.5	.405	117.7	.427
-.30	117.4	.418	118.0	.420	-1.0	118.5	.425	118.2	.432
-.40	117.0	.414	118.7	.427	-1.2	122.6	.466	123.2	.482
-.50	117.1	.415	119.1	.431	-1.4	126.8	.508	130.4	.554
-.60	117.5	.419	119.7	.437	-1.6	130.6	.546	133.0	.580
-.70	118.4	.429	119.6	.436	-1.8	133.1	.571	138.4	.634
-.80	117.9	.423	119.7	.437					
-.90	118.0	.425	122.6	.466					

Table 5.--Local cavity heat transfer ($h/b = 1.0$).

$h = \frac{q/A}{T_w - T_\infty} \quad (\text{BTU/hr.ft}^2 \text{ } ^\circ\text{F})$				
Upstream Wall	y/b	$\delta/b=0.16$	$\delta/b=0.28$	$\delta/b=0.36$
	-.0492	23.8	19.9	18.0
	-.1311	23.8	19.7	17.7
	-.2131	22.8	18.1	16.8
	-.2951	22.4	16.4	16.0
	-.3770	20.7	17.4	16.1
	-.4590	20.6	18.1	16.5
	-.5410	21.3	18.7	16.9
	-.6230	22.7	20.3	17.2
	-.7049	24.7	22.1	18.4
	-.7869	25.8	22.1	19.8
	-.8689	25.6	21.5	20.0
	-.9508	24.0	20.3	19.6
<u>Bottom</u>	x/b			
	.0492	22.4	19.0	18.4
	.1311	21.6	18.1	17.6
	.2131	21.6	18.1	17.8
	.2951	21.8	18.4	18.4
	.3770	22.2	19.0	18.8
	.4590	23.6	19.9	20.0
	.5410	24.4	21.5	22.0
	.6230	25.2	22.6	22.4
	.7049	26.5	24.1	24.0
	.7869	28.0	25.0	24.2
	.8689	26.6	24.5	22.0
	.9508	26.0	23.1	20.6
<u>Downstream Wall</u>	y/b			
	-.9508	24.0	53.5	38.2
	-.8689	23.7	49.2	33.9
	-.7869	23.8	42.6	29.0
	-.7049	24.0	30.4	28.5
	-.6230	24.5	26.9	26.0
	-.5410	26.4	24.3	24.3
	-.4590	31.6	22.4	23.4
	-.3770	35.3	21.5	22.6
	-.2951	48.4	20.8	20.0
	-.2131	54.3	20.3	19.8
	-.1311	62.1	20.0	19.0
	-.0492	63.4	20.8	19.0

Table 6.--Average cavity heat transfer.

$\frac{h}{b}$	u_{∞} ft./sec.	$\frac{\delta}{b}$	T_{∞} °F	T_w °F	T_o °F	Q BTU/HR	Stanton No. Based on ($T_o - T_{\infty}$)
							$\overline{St} = \frac{q/A}{\rho C_p u_{\infty} (T_o - T_{\infty})}$
0.50	70.6	.296	77.0	251.0	137.0	3460	.0483
0.50	76.0	.297	77.7	244.4	134.5	3210	.0447
0.50	106.0	.278	78.5	206.8	120.5	3175	.0416
0.50	71.5	.444	77.0	272.8	144.6	3320	.043
0.50	78.3	.446	77.0	270.0	143.2	3117	.0395
0.50	107.0	.417	77.0	232.5	129.4	3040	.0365
1.0	80.3	.559	76.5	272.0	156.1	3125	.0432
1.0	86.5	.572	76.5	273.7	158.3	3070	.039
1.0	92.1	.586	76.5	273.5	155.3	2985	.038
1.0	103.4	.373	77.5	208.2	134.5	3005	.0398
1.0	86.4	.386	77.5	229.8	143.0	2950	.0407
1.0	70.5	.400	77.5	249.2	152.0	2730	.0453
1.0	112.0	.161	77.0	157.6	108.5	2535	.0416
1.0	77.2	.173	77.0	194.7	120.0	2765	.0489
1.0	87.2	.162	77.0	182.5	116.0	2800	.0513
1.5	71.8	.60	78.0	293.4	160.5	1965	.0402
1.5	89.8	.574	78.0	218.8	135.8	2250	.044
1.5	110.3	.550	78.0	195.3	126.5	1740	.0378
1.5	84.3	.80	76.5	235.6	143.3	2170	.038
1.5	89.7	.78	76.5	237.7	142.7	2015	.036
1.5	104.3	.75	76.5	210.1	132.7	1875	.0365